Combustion and Flame 240 (2022) 112046

Contents lists available at ScienceDirect

Combustion and Flame

journal homepage: www.elsevier.com/locate/combustflame

Modeling of the effects of non-equilibrium excitation and electrode geometry on H_2/air ignition in a nanosecond plasma discharge

Xingqian Mao*, Hongtao Zhong, Tianhan Zhang, Andrey Starikovskiy, Yiguang Ju

Department of Mechanical and Aerospace Engineering, Princeton University, Princeton, NJ 08544, USA

ARTICLE INFO

Article history:
Received 17 July 2021
Revised 30 January 2022
Accepted 1 February 2022
Available online 17 February 2022

Keywords:
Plasma assisted ignition
Non-equilibrium excitation
Electrode geometry
Ignition kernel
Heat loss

ABSTRACT

This work presents the results of two-dimensional modeling of the effects of non-equilibrium excitation and electrode geometry on H_2/air ignition in a nanosecond plasma discharge. A multiscale adaptive reduced chemistry solver for plasma assisted combustion (MARCS-PAC) based on PASSKEy discharge modeling package and compressible multi-component reactive flow solver ASURF+ is developed and validated. This model is applied to simulate the impact of non-equilibrium plasma excitation and electrode geometry and heat loss on the dynamics of the discharge from streamer to spark and ignition kernel development in a H_2/air mixture with a pair of cylindrical electrodes. The results show that the plasma-generated species ($N_2(A)$, $N_2(B)$, $N_2(a')$, $N_2(C)$, $O(^1D)$, O and H) in the spark and afterglow significantly accelerate the ignition kernel development. The increase of discharge voltage at the same total discharge energy promotes the non-equilibrium active species production. It is found that the production of electronically excited species at higher reduced electric field strength is more efficient in enhancing ignition in comparison to the vibrational excitation and heating. Moreover, the 2D simulation clearly reveals that the electric field and active species distribution are highly non-uniform. The streamers are initiated at the sharp outer edges of the negative and positive electrodes by a strong electric field while the electric field is much weaker at the centerline of the electrodes. Furthermore, the simulations reveal that the ignition enhancement is sensitive to the variation of electrode shape, diameter, and gap size due to the changes of electric field distribution and location of streamer formation. A cylindrical electrode produces a larger discharge volume and ignition kernel than the parabolic and spherical electrodes, when the discharge is localized near the axis of the gap. It is found that there is a non-monotonic dependence of ignition kernel size on the electrode diameter and inter-electrode distance. The increase of electrode diameter and gap size above the optimal conditions leads to the reduction of ignition kernel volume, due to the decrease of active species concentration and gas temperature. At a larger electrode surface area and electrode diameter as well as smaller electrode gap size, the heat loss to electrode plays a greater role in reducing the ignition kernel size and slowing ignition kernel development. This work provides insights and guidance to understand the kinetic enhancement of non-equilibrium plasma and the effects of electrode geometries on ignition for the optimization ignitors in advanced engines.

1. Introduction

In recent years, non-equilibrium plasma has shown remarkable advantages in enhancing ignition [1–3], improving engine performance [4,5], extending flammability [6–10] and flame stabilization limits [11,12], accelerating low temperature fuel oxidation [13–18] and reforming [19–22] in internal combustion engines, high speed propulsion systems, and gas turbine engines [23,24]. Particularly, non-equilibrium short-pulsed plasma discharge has drawn great attention in the application of plasma assisted combustion [25,26]. Volumetric production of chemically active species and fast gas heating can be enabled by the non-equilibrium excitation effects of plasma in several nanoseconds due to a high reduced electric field (E/N, where E is the electric field and N is the gas number density), which significantly enhances ignition and combustion. However, the multi-timescale nature of localized streamer development as well as active species and heat production in plasma discharge requires quantitative understanding of the multi-dimensional dynamics of discharge development and the chemistry coupling between plasma and combustion.

To understand the underlying physical-chemical process of plasma assisted combustion, different numerical models and

* Corresponding author.
E-mail address: xingqian@princeton.edu (X. Mao).

https://doi.org/10.1016/j.combustflame.2022.112046
0010-2180/

experimental studies with zero-dimensional (0D) [16,17,27–31], one-dimensional (1D) [32–34], two-dimensional (2D) [35–41] and three-dimensional (3D) [42] discharges have been carried out. Although 0D and 1D models can provide critical information of plasma chemistry, they are not able to capture the dynamics of filament discharge development of plasma in practical engines in which multi-dimensional electrode geometries are used to optimize ignition enhancement. For example, the experiments conducted in propane/air mixtures by Lo et al. [43] and Pancheshnyi et al. [44] showed that the flame first appeared near the electrodes and then propagated along the inter-electrode and to the outside space in a point-to-plane discharge geometry. Moreover, the results showed that different configurations of the point-to-plane electrodes also affected the flame kernel size generation near the electrodes [43]. The experiments of CH_4/air ignition using nanosecond pulsed discharge in a convective flow by Lefkowitz and Ombrello [45,46] showed that the discharge inter-electrode distance also played an important role in the generation of effective ignition kernels. Furthermore, when the inter-electrode distance is varied, not only the electric field but also the heat loss to the electrode plays an important role to affect the ignition kernel development. Therefore, to understand the multi-dimensional discharge dynamics in plasma assisted ignition, it is necessary to model the plasma chemistry and filamentary plasma discharge development in a combustible mixture by using a multi-dimensional approach including the heat loss to the electrode.

In previous multi-dimensional modeling of plasma assisted combustion, Mahamud et al. [35] developed a 2D model to study the dual-pulse laser ignition in a CH_4/air ignition. As the model was designed for dual-pulse laser, the electric field and detailed plasma kinetics were not solved. Kobayashi et al. [36] studied the nanosecond discharges in H_2/air mixtures at atmospheric pressure. The results of species and temperature distributions between the point-to-point electrodes during and after the nanosecond voltage indicate that the non-uniformity in plasma affects the ignition enhancement and further studies of 2D reactive flow simulations are needed. Tholin et al. [37] conducted 2D simulations of the ignition of a lean premixed H_2/air flame between the point-to-point electrodes by a nanosecond spark discharge at atmospheric pressure with a reduced mechanism. Sharma et al. [38] developed a coupled 2D computational model of nanosecond pulsed plasma induced flame ignition and combustion between two cylindrical electrodes for a lean H_2/air mixture at high pressures using reactive compressible Euler equations without considering the detailed transport. Bechane and Fiorina [40] implemented a LES flow solver with semi-empirical model proposed by Castela et al. [41,42] to study the turbulent premixed flame ignition by nanosecond repetitively pulsed discharge without solving the electric field and detailed plasma chemistry. To summarize, the kinetic pathways of plasma-generated active species such as vibrationally and electronically excited species by the non-equilibrium excitation effects on ignition enhancement with detailed chemistry were rarely discussed in the framework of multi-dimensional models. Meanwhile, the effects of electrode geometry on discharge dynamics and ignition were rarely studied by modeling approach. Since both chemistry and transport are critical mechanisms for ignition and flame propagation, the development of a multi-dimensional plasma assisted combustion model with detailed chemistry and transport is still of great interest.

Recently, an experimentally validated 2D plasma solver PASSKEy (PArallel Streamer Solver with KinEtics) [47] shows a good performance in modeling streamer-to-spark transition of the plasma discharge [48]. The solver was originally designed for nanosecond surface discharges [49] and later extended for other discharge modeling [50–52], but the code does not include combustion chemistry. On the other hand, for detailed adaptive combustion chemistry and transport modeling, an adaptive simulation of unsteady reactive flow solver ASURF+ [53–56] has been developed, validated, and widely used in modeling of unsteady ignition and flame propagation. Therefore, PASSKEy and ASURF+ provide validated computational platforms to develop a 2D computational tool for plasma assisted combustion and reforming with detailed chemistry and transport.

In this study, firstly, a new two-dimensional multi-scale adaptive reduced chemistry solver for plasma assisted combustion (MARCS-PAC) is developed and validated by integrating PASSKEy and ASURF+ solvers. Secondly, plasma assisted ignition development in a H_2/air mixture with a nanosecond discharge between a pair of cylindrical electrodes is studied by MARCS-PAC with detailed combustion chemistry and transport. The effects of non-uniform distributions of electric field, electron number density, excited species, radicals, and energy release generated by pulsed discharge on ignition are modeled. Then, voltage and electric field effects on non-equilibrium excitation of plasma and ignition chemistry between the two electrodes are investigated. Finally, the effects of electrode geometries including the electrode shape, diameter, and gap size as well as the heat loss to the electrode on ignition enhancement are studied.

2. Numerical methods

The two-dimensional multi-scale adaptive reduced chemistry solver for plasma assisted combustion (MARCS-PAC) integrates the 2D plasma solver PASSKEy [47–52] and the adaptive simulation of unsteady reactive 2D flow solver ASURF+ [53–56]**.** The governing equations, chemistry, and transport properties of a multi-component, compressible reactive flow and the time splitting solution methods are summarized here.

2.1. Governing equations

The PASSKEy code solves the continuity equation for the species such as electrons, ions, vibrationally and electronically excited molecules, intermediate species, reactants and products in plasma [49],

$$\frac{\partial n_k}{\partial t} + \vec{\nabla} \cdot \vec{J_k} = S_k + S_{\text{ph}} \tag{1}$$

where n_k is the number density of species k, t the time, $\vec{J_k}$ the flux vector of species k due to drift-diffusion of charged species in local self-consisted electric field, and S_k and S_{ph} the production or consumption rate of species k contributed by plasma kinetics and photoionization, respectively.

The flux vector $\vec{J_k}$ is obtained by the drift-diffusion approximation,

$$\vec{J_k} = z_k \mu_k n_k \vec{E} - D_k \vec{\nabla} n_k \tag{2}$$

where z_k is the charge number of species k, μ_k and D_k the mobility and the diffusion coefficient of charged species, respectively, and $\vec{E}$ the electric field vector.

Due to the lack of an appropriate photoionization model of $H_2/O_2/N_2$ mixtures, it is assumed that the photoelectrons come from the ionization of O_2 molecules by vacuum ultraviolet (VUV) radiation from electronically excited N_2. In [39] it was shown that the influence of H_2 absorption could be taken into account adding an additional absorption in photoionization term. It was also shown that the VUV radiation absorption by hydrogen plays a minor role in streamer discharge propagation and plasma channel development [39]. The photoionization source term is calculated by the three-term Helmholtz equations [57,58],

$$S_{\text{ph}} = \sum_j S_{\text{ph}}^{\ j} \tag{3}$$

$$\vec{\nabla}^2 S_{\mathrm{ph}}^{\ j} - \left(\beta_j p_{\mathrm{O_2}}\right)^2 S_{\mathrm{ph}}^{\ j} = -B_j p_{\mathrm{O_2}}^2 I_{\mathrm{ph}} \tag{4}$$

where $S_{\mathrm{ph}}^{\ j}$ is the three-exponential fit term ($j = 3$) for photoionization rate, β_j and B_j the fitting coefficients for photoionization functions, $p_{\mathrm{O_2}}$ the partial pressure of O_2, and I_{ph} the photons production rate.

The electric potential is calculated by Poisson's equation,

$$\vec{\nabla} \cdot (-\varepsilon_0 \varepsilon \vec{\nabla} \varphi) = \mathrm{q_e} \sum_k z_k n_k \tag{5}$$

where ε_0 is the permittivity of free space (8.8542×10^{-12} F·m^{-1}), ε the relative dielectric constant, φ the electric potential ($\vec{E} = -\vec{\nabla}\varphi$), and $\mathrm{q_e}$ the absolute value of electron charge (1.602×10^{-19}C).

Gas heating in the discharge is calculated by the method of Flitti and Pancheshnyi [59]. The external electric power deposited to plasma per unit volume, P_{ext}, is calculated by,

$$P_{\mathrm{ext}} = \vec{j_c} \cdot \vec{E} \tag{6}$$

where $\vec{j_c} = -\mathrm{q_e}\vec{J_e}$ is the conductive current density vector, and $\vec{J_e}$ is the electron flux vector. The electric power deposited in the plasma are comprised of three parts [59]: the power distributed respectively to the translational degree of freedom of electrons P_{elec}, the translational degree of freedom of gas P_{gas}, and the internal degree of freedom of gas P_{int}. Therefore, the gas heating P_{gas} from plasma is calculated by,

$$P_{\mathrm{gas}} = P_{\mathrm{ext}} - P_{\mathrm{elec}} - P_{\mathrm{int}} \tag{7}$$

$$P_{\mathrm{elec}} = \frac{3}{2}\mathrm{k_B}\frac{\mathrm{d}(n_e T_e)}{\mathrm{d}t} \tag{8}$$

$$P_{\mathrm{int}} = \sum_k \epsilon_k \frac{\mathrm{d}n_k}{\mathrm{d}t} \tag{9}$$

where $\mathrm{k_B}$ is the Boltzmann constant (1.38×10^{-23} J·K^{-1}), n_e the electron number density, T_e the electron temperature (unit in K), and ϵ_k the internal energy of species k.

The conductive current I is obtained from the conductive current density by

$$I = \int \vec{j_c} \cdot \vec{n}\, \mathrm{d}A \tag{10}$$

where $\vec{n}$ is the normal direction vector, and A is the surface area of electrode.

The rate constants of electron impact reactions, the transport parameters for electrons, and the mean electron energy are precalculated by using BOLSIG+ [60]. The cross-section data of electron impact reactions are obtained from the online database LXCat [61]. The electron temperature during the discharge is obtained by solving the Boltzmann equation with the local field approximation [60,62].

The discharge development solution is coupled with the unsteady, multi-component, reactive, compressible Navier-Stokes (N-S) reactive 2D flow solver ASURF+ [53–56]. The two-dimensional axisymmetric conservation equations of mass, momentum and energy at the cylindrical coordinates are listed as follows [53],

$$\frac{\partial \rho}{\partial t} + \vec{\nabla} \cdot \left(\rho \vec{V}\right) = 0 \tag{11}$$

$$\frac{\partial \left(\rho \vec{V}\right)}{\partial t} + \vec{\nabla} \cdot \left(\rho \vec{V}\vec{V}\right) = -\vec{\nabla} p + \vec{\nabla} \cdot \bar{\bar{\tau}} \tag{12}$$

$$\frac{\partial e}{\partial t} + \vec{\nabla} \cdot \left((e+p)\vec{V}\right) = -\vec{\nabla} \cdot \vec{q} + \vec{\nabla} \cdot \left(\bar{\bar{\tau}}\vec{V}\right) + P_{\mathrm{gas}} \tag{13}$$

where ρ is the gas mass density, $\vec{V}$ the velocity vector, p the pressure, $\bar{\bar{\tau}}$ the viscous stress tensor, e the total energy per unit volume, and $\vec{q}$ the heat flux vector. The gas heating P_{gas} from plasma is a source term of Eq. (13).

The conservation equation of species k consisting both plasma and combustion kinetics is given as,

$$\frac{\partial (\rho Y_k)}{\partial t} + \vec{\nabla} \cdot \left[\rho\left(\vec{V} + \vec{V_k}\right) Y_k\right] = \omega_k \tag{14}$$

$$\omega_k = \omega_k^{\mathrm{plasma}} + \omega_k^{\mathrm{combustion}} \tag{15}$$

$$\omega_k^{\mathrm{plasma}} = S_k + S_{\mathrm{ph}} - \vec{\nabla} \cdot \vec{J_k} \tag{16}$$

where Y_k and $\vec{V_k}$ are the mass fraction and the diffusion velocity of species k, respectively, and ω_k is the production or consumption rate of species k contributed, respectively, by plasma discharge $\omega_k^{\mathrm{plasma}}$ and combustion kinetics $\omega_k^{\mathrm{combustion}}$.

The summation of the conservation equations of all species needs to recover to the mass conservation Eq. (11) and thus requires,

$$\sum_k \omega_k = 0 \tag{17}$$

$$\sum_k \left(\rho Y_k \vec{V_k}\right) = 0 \tag{18}$$

The diffusion velocity vector $\vec{V_k}$ is obtained by the summation of the ordinary diffusion velocity $\vec{V_{k,Y}}$ given in the Curtiss-Hirschfelder approximation, the thermal diffusion velocity $\vec{V_{k,T}}$ as well as the correction velocity $\vec{V_{k,C}}$ which insures the compatibility of species and mass conservation equations [63],

$$\vec{V_k} = \vec{V_{k,Y}} + \vec{V_{k,T}} + \vec{V_{k,C}} \tag{19}$$

The heat flux term $\vec{q}$ in Eq. (13) includes a heat diffusion term calculated by the Fourier's Law and a term of the diffusion of species with different species enthalpies,

$$\vec{q} = -\lambda \vec{\nabla} T + \rho \sum_k \left(h_k Y_k \vec{V_k}\right) \tag{20}$$

where λ is the thermal conductivity of the mixture, T is the gas temperature, and h_k is the enthalpy of species k.

The N-S equations are closed by the equation of state,

$$p = \rho \mathrm{R^0} T / \bar{M} \tag{21}$$

where $\mathrm{R^0}$ is the universal gas constant (8.314 J·mol^{-1}·K^{-1}), and $\bar{M}$ is the mean molecular weight of the mixture.

2.2. Numerical schemes

The finite volume method is used for discretizing the above governing equations. A detailed description of the numerical schemes for plasma modeling of PASSKEy has been described in [49]. The Poisson's equation and Helmholtz equations are solved by a preconditioned conjugate-gradient solver [64,65]. A semi-implicit time integration scheme is applied for Poisson's equation [66,67].

Table 1
Species in the kinetic model.

Molecules	Radicals	Excited species	Charged species
H_2, O_2, N_2, H_2O, H_2O_2, O_3, NO, NO_2, N_2O, HNO, HONO	H, O, N, OH, HO_2, NH	$H_2(v{=}1)$, $O_2(v{=}1)$, $N_2(v{=}1)$, $O_2(a^1\Delta_g)$, $O_2(b^1\Sigma_g^+)$, $O(^1D)$, N_2(A), N_2(B), $N_2(a')$, N_2(C), $N(^2D)$	H_2^+, O_2^+, N_2^+, N_4^+, O^-, O_2^-, e

(N_2(A) is the summation of $N_2(A^3\Sigma_u^+, v=0-4)$, $N_2(A^3\Sigma_u^+, v=5-9)$ and $N_2(A^3\Sigma_u^+, v=10-)$; N_2(B) is the summation of $N_2(B^3\Pi_g)$, $N_2(W^3\Delta_u)$ and $N_2(B'^3\Sigma_u^-)$; $N_2(a')$ is the summation of $N_2(a'^1\Sigma_u^-)$, $N_2(a^1\Pi_g)$ and $N_2(w^1\Delta_u)$; N_2(C) is the summation of $N_2(C^3\Pi_u)$, $N_2(E^3\Sigma_g^+)$ and $N_2(a''^1\Sigma_g^+)$).

The drift term of charged species is solved by an explicit UNO3 scheme [68]. The plasma chemistry is calculated by the stabilized Runge-Kutta-Chebyshev (RKC) method [69]. In ASURF+ [53–56], the combustion kinetics and the transport coefficients are calculated by the CHEMKIN-TRANSPORT packages [63,70]. The convection fluxes in Eqs. (11)–(14) are solved by either HLLC scheme [71] or the WENO scheme [72,73] in ASURF+. The HLLC scheme is used in this study. The central difference scheme is applied to evaluate the diffusive flux. In the present solver, the 3rd Runge-Kutta scheme is used in time integration. Theses numerical schemes for the calculation of combustion chemistry, convection and diffusion terms were validated by ignition delay, shock wave, and flame propagation, which can be found in supplementary materials. The correlated dynamic adaptive chemistry and transport (CO-DACT) method [74] and the hybrid multi-timescale (HMTS) [75] modules are adopted to improve computational efficiency. To solve the conservation Eqs. (11)–(14), the stiff source terms P_{gas} of Eq. (13) and ω_k of Eq. (14) are solved by fractional-step time-splitting method [71]. At each time-step, at first, the governing equations of plasma discharge involving electric field, P_{gas} and ω_k^{plasma} are solved. Then, the combustion kinetics involving $\omega_k^{\text{combustion}}$ are solved. Finally, the convection and diffusion terms are solved and all the parameters are updated for the next time step. The simulations were performed using 2.4 GHz Intel Broadwell processor with 128 GB memory per node. Each case takes 96–120 h with 16 CPU cores.

2.3. Plasma assisted $H_2/O_2/N_2$ combustion kinetic model

A modified plasma assisted $H_2/O_2/N_2$ combustion kinetic model from [31] is used in this work. The mechanism consists of a plasma sub-model and a combustion sub-model. The mechanism consists of 35 species. The plasma sub-model has 68 reactions and the combustion sub-model has 81 reactions. The species included in the mechanism are listed in Table 1. The plasma sub-model was reduced from the detailed plasma kinetic model originally from [31]. The detailed description about the model reduction process can be found in supplementary materials. The plasma sub-model incorporates the reactions of electron impact vibrational excitation, electronic excitation, dissociation, ionization and attachment, as well as quenching of vibrationally and electronically excited species, charge exchange, electron detachment, ion-ion and electron-ion recombination. The cross-section data of H_2 and N_2 were taken from the Phelps database [76], and the cross sections of O_2 were obtained from the Biagi database [77]. Note that the ionization cross sections of H_2 were obtained from the IST-Lisbon database [78] which provides more detailed data for different electron energies. For the combustion sub-model, a detailed $H_2/O_2/N_2$ combustion mechanism from HP-Mech [79] with NO_x formation [80,81] and O_3 sub-mechanisms [82] was used.

2.4. Initial and boundary conditions

For the initial condition, a uniform pre-ionized $H_2/O_2/N_2$ mixture was used for the simulation. The initial electron number density is 10^4 cm^{-3} [36,83,84], and the same initial ion density is given based on quasi-neutrality. All the simulations were conducted in a stoichiometric H_2/air mixture (0.296 H_2/0.148 O_2/0.556 N_2) at 800 K and atmospheric pressure. A nanosecond discharge with a single pulse was used to study the plasma assisted ignition. For simplicity, a trapezoidal waveform voltage ranging from 2000 to 5000 V with a rise time of 2 ns was applied to the electrodes. The end time of nanosecond discharge is controlled by the total deposited energy in plasma which is set as 0.4 mJ for all simulations.

For the boundary conditions of the electric potential, $\varphi = U(t)$ was used for metal surface and $\partial\varphi/\partial n = 0$ was used for non-metal boundary of the Poisson's equation. For the drift-diffusion equations of charged species, the boundary condition for the electron flux at the metal was $\partial J_e/\partial n = 0$. The settings of $\partial J_i/\partial n = 0$ and $J_i = 0$ were applied for the ions flowing in and flowing out the metal surface, respectively. For the N-S equations, the transparent boundary conditions were applied for external boundaries and the reflective boundary conditions were applied for electrodes. Two cases of heat losses were considered: adiabatic case assumed that there is no heat loss at electrodes. For non-adiabatic regime, a conduction heat transfer to the cold electrodes with a constant temperature of $T_{\text{electrode}} = 300$ K was incorporated. The value $T_{\text{electrode}} = 300$ K increases the cooling effect and was used to demonstrate the influence of the heat transfer on the ignition kernel development.

2.5. Electrode geometry and computational domain

The electrode geometries of anode and cathode in this study were axisymmetric. The *R*-axis of the cylindrical coordinates indicates the direction of electrode radius and the *Z*-axis indicates the direction of electrode length. The electrode shape, diameter, and the gap size were varied to study the effect of electrode geometry on ignition. A computational domain of 5×10 mm^2 was used in the simulation. To reduce the computational cost, a fine and uniform orthogonal mesh (10×10 μm) was used in the center region of plasma discharge and ignition kernel formation. In the outer region, the mesh size increases exponentially, as shown in Fig. 1. The time step is limited by the shortest characteristic timescale of the drift dynamics of charged species, plasma kinetics, combustion kinetics, and fluid dynamics for all grids.

3. Results and discussion

3.1. 2D effects of plasma discharge on ignition

Streamer propagation, its transition to spark and the ignition kernel development were performed in the framework of 2D model described above. In the first series of calculations, the electrode diameter was 2 mm and the gap size between anode and cathode was 2 mm. The applied voltage was 5000 V with a rise time of 2 ns. The system was assumed as adiabatic. Figure 2 shows the applied voltage pulse shape and calculated dynamics of the discharge current.

During the first nanosecond, the electric field in the gap is too low for the development of ionization, and the discharge cur-

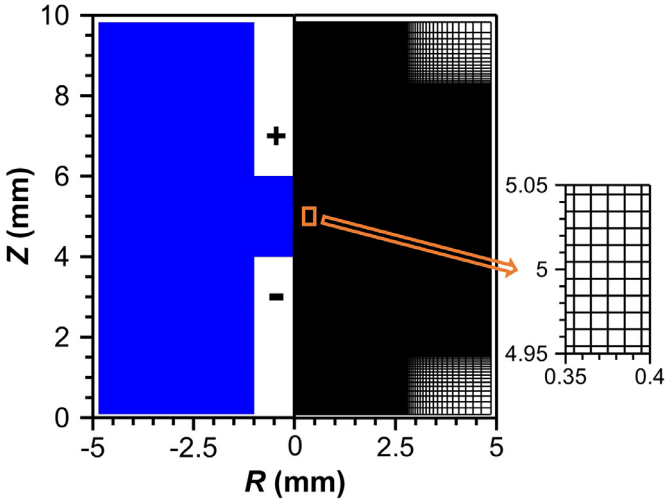

Fig. 1. Computational domain, geometry and mesh distribution.

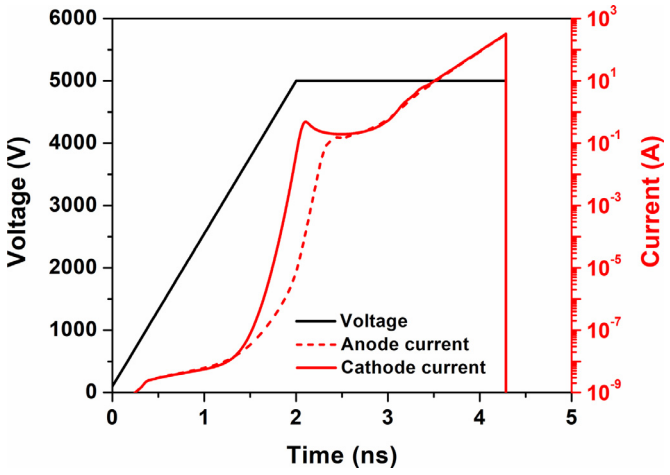

Fig. 2. Applied voltage and calculated dynamics of the discharge current.

rent is determined by the initial ionization of the gas in the gap ($n_e(0) = 10^4$ cm^{-3}) and the drift of electrons in a weak electric field. As the voltage on the electrodes increases, the development of ionization waves begins in the gap ($t > 1.5$ ns, Fig. 2). The discharge current during this phase is closed by displacement currents, since the gap remains open. After $t = 2$ ns, when the voltage on the electrodes stops growing, a redistribution of potentials in the plasma occurs, leading to a local decrease in the electric fields near the electrodes and a decrease in the discharge current. Subsequently ($t = 3$ ns), the gap is bridged, the electric field at all points of the plasma becomes higher than the critical one, which leads to a rapid increase in the plasma density and conductivity at $t > 3.5$ ns.

Figures 3(a–f) show the time evolutions of E/N, electron temperature, electron number density, mole fractions of the atomic oxygen in excited O(^{1}D) and ground state O(^{3}P), as well as gas temperature during plasma assisted H_2/air ignition. Figs. 3(a,b) show that the highest electric field and electron temperature are first generated near the edges of the electrodes due to the local electric field enhancement. During initial stage of the discharge, a high electric field (up to $E/N \sim 1000$ Td) is generated near the edge of the electrode, as shown in Figs. 3(a), 4(a). Figures show that the ionization waves start at the cathode edges. The streamers from the anode develop much slower because they require the photoelectrons production in front of the ionization waves ($t = 2.5$ and 3.0 ns in Fig. 3(c)). After bridging the gap, the negative and positive streamers merged, and the electric field distribution in the discharge gap becomes more uniform. After that, the streamers transform to a nanosecond spark. The ionization of the gas increases, and the energy is rapidly deposited into plasma. This is also observed by the current increase after $t = 3$ ns in Fig. 2. During this stage, the major portion of excited species and radicals such as O(^{1}D) and O are produced because of the high electron number density, especially in the discharge channel near the edges of the electrode, as shown in Figs. 3(d,e) and 4(b).

When the total discharge energy reaches $Q = 0.4$ mJ, the voltage on the electrodes is set to zero (Fig. 2). Discharge stops, and the afterglow stage begins. In this afterglow stage, the electron density and O(^{1}D) mole fraction decrease gradually (Fig. 3(c) and (d)). Plasma recombination is controlled by the electron-ion dissociative recombination and electron attachment reactions; decrease in excited oxygen density is due to the collisional quenching of O(^{1}D) by hydrogen and nitrogen molecules.

The temperature profile at $t = 30$ μs in Fig. 3(f) shows that the ignition kernel is firstly formed near the electrode edges because of the high concentrations of excited species and radicals as well as the fast temperature increase in the regions of high electric fields and high energy density of the discharge. The initial ignition kernel volume is larger at the cathode because of shorter start delay time for negative streamers (Fig. 3(c)). After that, the ignition kernel propagates into the unburned gas regions near the electrodes. The density of radicals generated during ignition increases rapidly, such as the time evolution of O radical shown in Fig. 3(e). With the ignition kernel propagation, a large volume of high-temperature burned gas is formed, as shown in the temperature profile at $t = 90$ μs (Fig. 3(f)).

Therefore, the active species production, gas heating and ignition dynamics significantly vary in 2D-space. Thus, quantitative model of spark ignition in engines should consider the multi-dimensional effects of plasma initiation, streamer propagation, and non-uniform distribution of active species production between the electrodes.

Figures 5(a) and (b) present the spatial distributions of species mole fraction and gas temperature between anode and cathode at the electrodes edge ($R = 1$ mm) along Z-axis and at the center of discharge gap ($Z = 5$ mm) along R-axis, respectively. The data are analyzed at the end of high-voltage pulse ($t = 4.3$ ns). It is observed that the discharge cross-section near the electrodes is smaller than that in the middle of discharge gap (Fig. 3(c)). This leads to higher conductive current density and specific energy deposition, and thus increases active species concentrations and temperature close to the electrodes. Because more electrons and active species are generated near the cathode, the gas temperature is higher compared with anode region (Fig. 5(a)). Fig. 5(b) shows that a considerable number of excited species and radicals are produced in the discharge gap between anode and cathode ($R < 1.3$ mm). The species mole fractions and temperature reach to the peak at the electrode edges around $R = 1.0$ mm and decrease significantly at the outside of the electrode where the electric field is weak. Among these plasma-generated species, H and O radicals, vibrationally excited species $N_2(v = 1)$ as well as electronically excited species such as O(^{1}D) and N_2(B) are produced significantly.

To understand the kinetic effects of plasma-generated species on ignition enhancement, the time evolutions of species mole fractions and temperature during plasma assisted ignition process are presented in Figs. 6(a) and (b) for a point near the anode in the region of the most intensive discharge energy release ($R = 1$ mm, $\Delta Z = 5$ μm from anode). The major electron impact reactions in nanosecond discharge from the point of view of ignition development are processes of vibrational excitation of nitrogen, excitation of electronic degrees of freedom, and direct dissociation and ion-

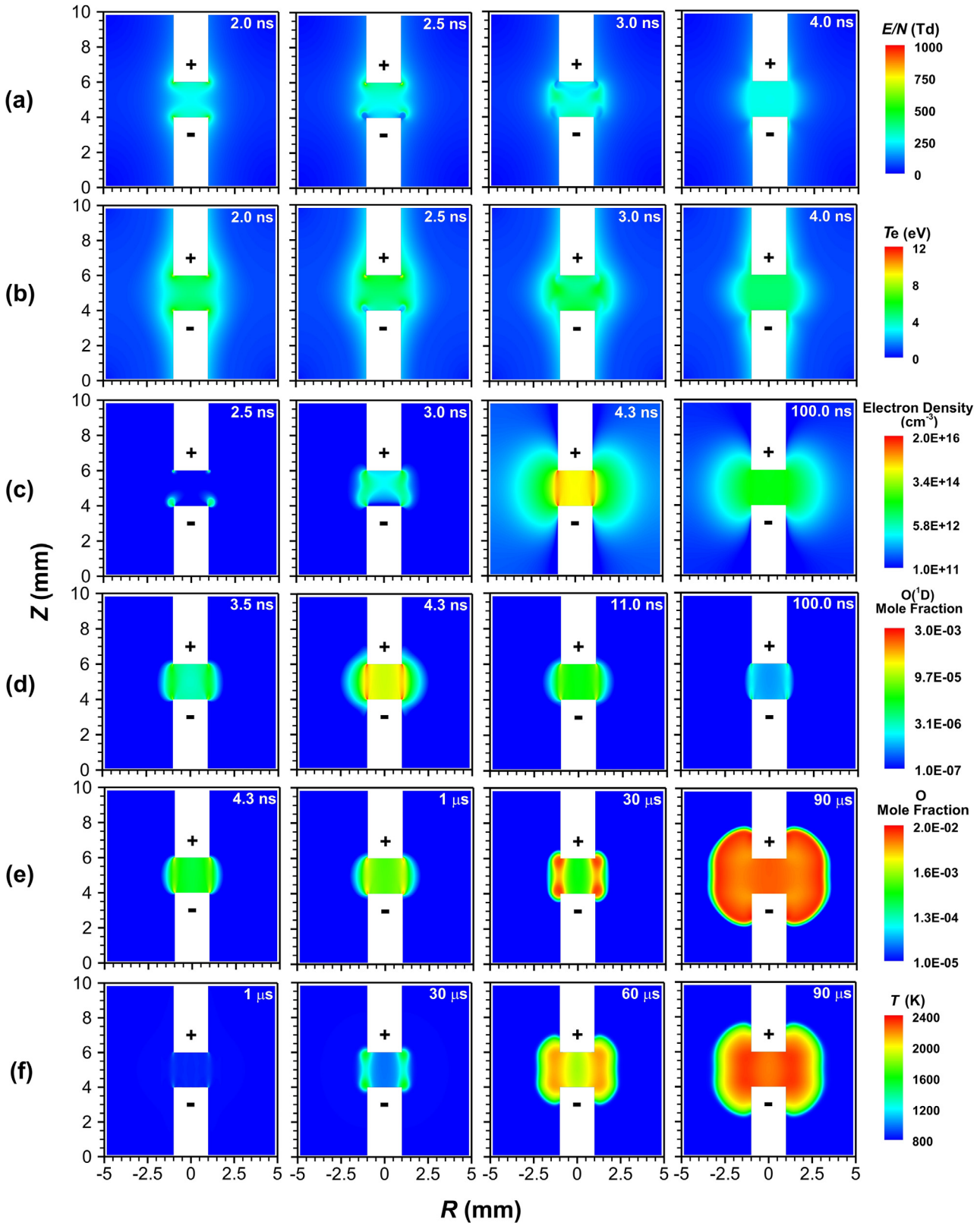

Fig. 3. Time evolutions of E/N, electron temperature, electron number density, mole fractions of excited species $O(^1D)$ and O radical, as well as gas temperature during plasma assisted H_2/air ignition at $U = 5000$ V.

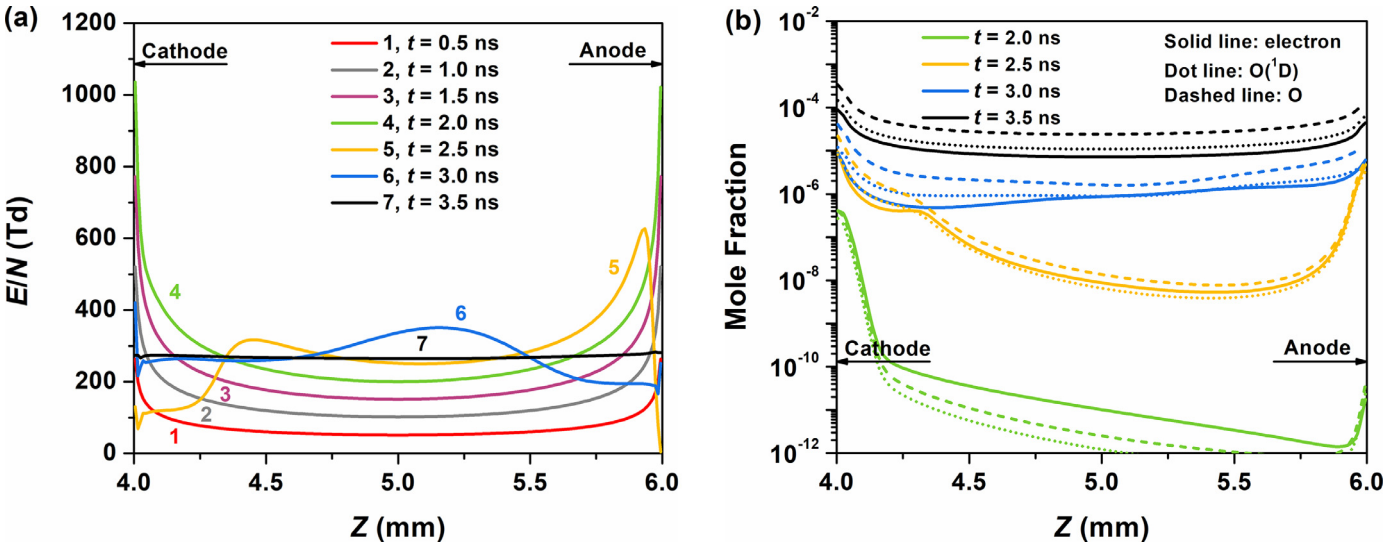

Fig. 4. Time evolutions of (a) E/N and (b) mole fractions of electron, O(^{1}D) and O between anode and cathode along Z-axis at R = 1 mm.

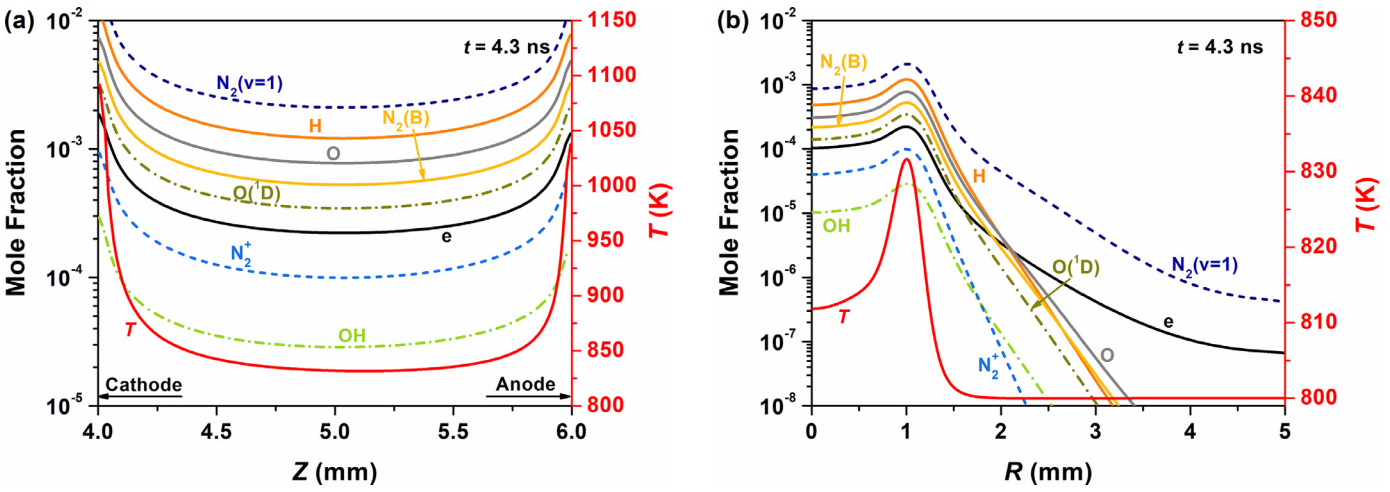

Fig. 5. Spatial distributions of species mole factions and gas temperature between anode and cathode (a) at the electrodes edge (R = 1 mm) along Z-axis and (b) at the center of discharge gap (Z = 5 mm) along R-axis at t = 4.3 ns.

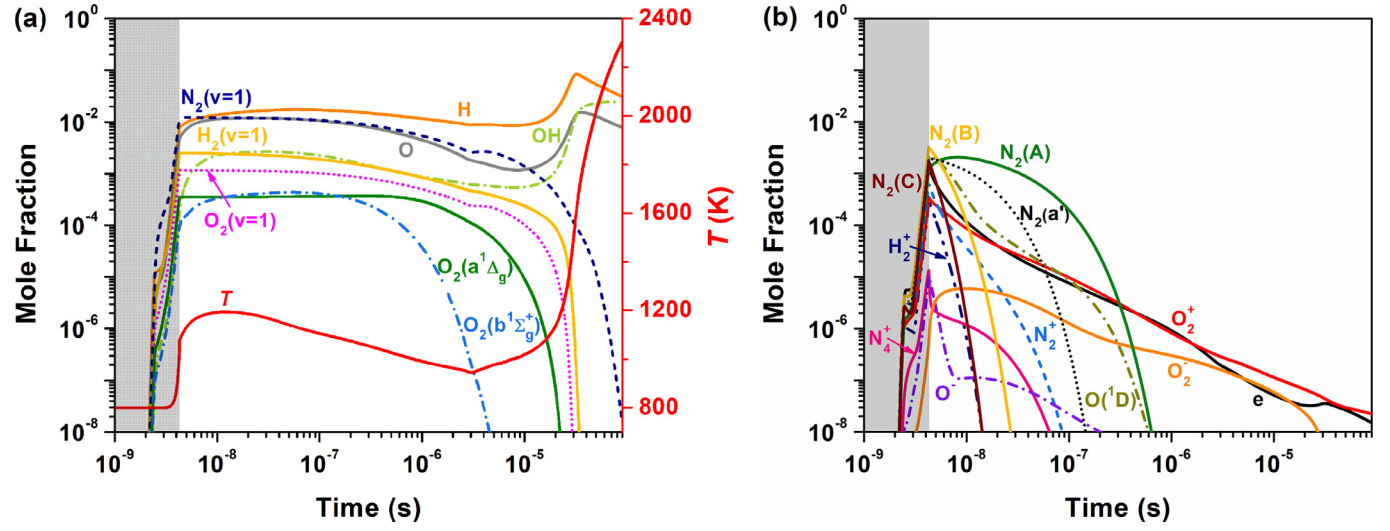

Fig. 6. Time evolutions of species mole fractions and temperature during plasma assisted ignition at the location R = 1 mm, ΔZ = 5 μm from anode. Gray shadow marks the discharge phase.

ization of molecules by electron impact:

$$e + N_2 \rightarrow e + N_2(v = 1) \quad (R1)$$

$$e + N_2 \rightarrow e + N_2(A)/N_2(B)/N_2(a')/N_2(C) \quad (R2)$$

$$e + H_2 \rightarrow e + H + H \quad (R3)$$

$$e + O_2 \rightarrow e + O + O \quad (R4)$$

$$e + O_2 \rightarrow e + O + O(^1D) \quad (R5)$$

$$e + M \rightarrow e + e + M^+ (M = H_2, O_2, N_2) \quad (R6)$$

For the primary radical production such as H and O in plasma discharge, Fig. 6(a) shows the time histories of H and O concentrations. It is seen that the radical concentrations increase rapidly during the plasma discharge in the timescale of ~ 10 ns. Besides the electron impact dissociation reaction (R3), the production of H is mainly contributed by the collisions of electronically excited species $N_2(a')$, $N_2(C)$ and $O(^1D)$ via

$$N_2(a') + H_2 \rightarrow N_2 + H + H \quad (R7)$$

$$N_2(C) + H_2 \rightarrow N_2 + H + H \quad (R8)$$

and

$$O(^1D) + H_2 \rightarrow H + OH \quad (R9)$$

The major reactions of O atoms production are reactions (R4), (R5) and collisional quenching of nitrogen triplet states:

$$N_2(B) + O_2 \rightarrow N_2 + O + O \quad (R10)$$

$$N_2(C) + O_2 \rightarrow N_2 + O + O(^1D) \quad (R11)$$

These reactions also provide fast gas heating and raise the temperature during plasma discharge and in the early afterglow [85–88], as shown in Fig. 6(a). The radical production and fast heating accelerate the ignition process and lead to branched-chain thermal explosion development.

The time histories of major electronically excited species are shown in Fig. 6(b). It is seen that $N_2(B)$ and $N_2(C)$ are quickly quenched in ~ 20 ns by molecular oxygen and hydrogen. $N_2(B)$ contributes to O production through (R10) and is also converted into $N_2(A)$ via

$$N_2(B) + N_2 \rightarrow N_2(A) + N_2 \quad (R12)$$

and

$$N_2(B) + H_2 \rightarrow N_2(A) + H_2 \quad (R13)$$

leading to the increase of $N_2(A)$ in the early stage of afterglow.

$O(^1D)$ is mainly produced in reactions (R5) and (R11) and consumed quickly in (R9) to generate H and OH radicals during discharge phase and early afterglow. The production of $O(^1D)$ has a strong kinetic enhancement on fuel oxidation at low temperatures [2]. In the late afterglow, $O(^1D)$ concentration decrease slows down due to its production from $N_2(a')$ in reactions with O_2 as well as the recombination reaction between electron and O_2^+

$$N_2(a') + O_2 \rightarrow N_2 + O + O(^1D) \quad (R14)$$

$$e + O_2^+ \rightarrow O + O(^1D) \quad (R15)$$

$N_2(A)$ is consumed in reactions of collisional quenching

$$N_2(A) + H_2 \rightarrow N_2 + H + H \quad (R16)$$

and

$$N_2(A) + O_2 \rightarrow N_2 + O + O \quad (R17)$$

It is noted that the concentration of vibrationally excited nitrogen $N_2(v = 1)$ is also significant in the plasma. Fig. 6(a) shows that $N_2(v = 1)$ has a long lifetime (~ 20 μs). However, it is mainly consumed by vibrational-translational (VT) relaxation reaction [2]:

$$N_2(v = 1) + H_2 \rightarrow N_2 + H_2 \quad (R18)$$

The vibrationally excited hydrogen $H_2(v = 1)$ and oxygen $O_2(v = 1)$ consumed by

$$O + H_2(v = 1) \rightarrow H + OH \quad (R19)$$

$$H_2(v = 1) + OH \rightarrow H_2O + H \quad (R20)$$

and

$$H + O_2(v = 1) \rightarrow O + OH \quad (R21)$$

also accelerate the radical production, but their kinetic effects on ignition enhancement are minor due to low concentrations.

From the discussion above, the different spatial distribution and time evolution of plasma properties show that multi-dimensional models are required to quantitatively model plasma assisted spark ignition. Therefore, in the following sections, we will examine the effects of applied voltage and electrode geometry on plasma dynamics and ignition enhancement. The ideally symmetric electrode geometry is difficult to be achieved in a real engine, and was used as an approximation to demonstrate the role of volumetric excitation of the mixture. The asymmetry in electrode's configuration and the discharge instabilities development will lead to the asymmetric energy distribution in plasma. Generally the higher energy density will increase the ignition but the smaller ignition kernel will delay the combustion wave propagation.

3.2. Voltage effects on non-equilibrium excitation and ignition chemistry

As E/N is an important parameter in a plasma discharge which controls the electron energy, energy transfer, and the production of excited species [2], in this section, we examine how the discharge voltage affects non-equilibrium excitation in the nanosecond discharge and ignition chemistry. The cylindrical electrode geometry and gap size were kept the same, but the applied peak pulse voltage was increased from 2000 to 5000 V with the same deposited discharge energy of 0.4 mJ.

The fractions of energy deposited into different molecular degrees of freedom in the stoichiometric H_2/air (0.296 H_2/0.148 O_2/0.556 N_2) mixture as a function of E/N were calculated, for example, in [2]. The results show that most energy is transferred to the rotational excitation and vibrational excitation of $O_2(v)$ and $H_2(v)$ at electric field below 10 Td (1 Td = 10^{-17} V·cm^2). Between 10 and 100 Td, the energy is mainly transferred to $N_2(v)$ and a part of energy goes to the electronic excitation of N_2 as well as the dissociation of O_2 and H_2. As the E/N further increases above 100 Td, the electronic excitation of N_2 and dissociation and ionization of H_2, O_2 and N_2 dominate the discharge but the energy deposition in the vibrational excitation mode decreases.

Figure 7 shows the comparison of ignition kernel volume at $t = 90$ μs and the corresponding chemical heat release during the plasma assisted H_2/air ignition process with different peak pulse voltages. The ignition kernel volume is defined as the integration

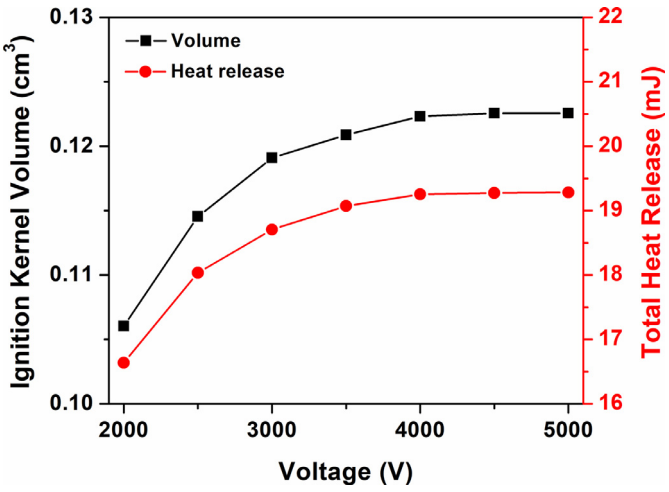

Fig. 7. Ignition kernel volume at $t = 90$ μs and total chemical heat release in plasma assisted H_2/air ignition with different peak pulse voltages.

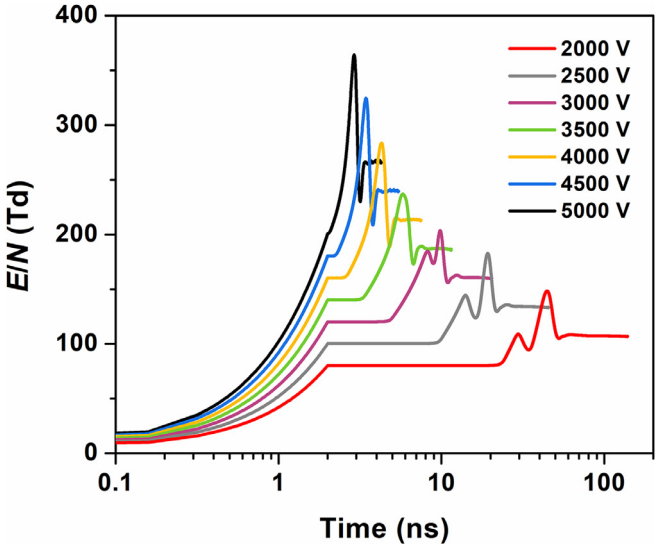

Fig. 8. Time evolutions of E/N with different peak pulse voltages at the location of ($R = 1$ mm, $Z = 5$ mm).

of the volume with a temperature rise of 400 K above the initial temperature. The total heat release is integrated over the whole computational domain during 90 μs. The results show that although the ignition kernel volume and total heat release change slightly from 5000 to 4000 V, they decrease noticeably when the peak voltage is below 4000 V at the same discharge energy 0.4 mJ, indicating that the efficiency of ignition by pulsed discharge is reduced with the voltage decrease. This decrement further accelerates when the peak pulse voltage drops below 3000 V. As it will be discussed later, the decrease could be explained by discharge energy redistribution from electronically excited to vibrationally excited species production at low E/N (see, for example, discussion in [2]).

Figure 8 shows the time evolutions of E/N with different voltages at the coordinates of ($R = 1$ mm, $Z = 5$ mm), which is located at the center of the discharge gap in the vertical direction of the outer electrode edges. The results show that with a lower input voltage, the E/N in the discharge gap decreases and the transition to the spark takes a longer time. The active species production during the nanosecond discharge is mainly dominated by the main, most powerful, stage of the discharge after the streamers bridge the gap. The comparison of active species (such as electrons, $N_2(B)$, $O(^1D)$, H, O and $N_2(v = 1)$) mole fractions at the location of ($R = 1$ mm, $Z = 5$ mm) with different pulse voltages is shown in Fig. 9(a)–(f). Figure 9(a) demonstrates that at $U = 5000$ V a high concentration of electrons can be produced in a short period of time when discharge develops at high E/N and more discharge energy is deposited to ionization. The peak mole fractions of electronically excited species $N_2(B)$ and $O(^1D)$ produced in plasma are similar between 4000 and 5000 V (the corresponding E/N value after bridging the gap is between 210 and 270 Td). However, for a peak pulse voltage below 3000 V, especially at 2000 V, the results show that the maximal mole fractions of $N_2(B)$ and $O(^1D)$ decrease significantly during the discharge phase while the vibrationally excited molecule $N_2(v = 1)$ becomes the major species generated in plasma as more energy is deposited to the vibrational degrees of freedom. The production of other electronically excited states of $N_2(A)$, $N_2(a')$ and $N_2(C)$ also decreases below $U = 4000$ V. The peak concentrations of H and O atom do not vary significantly because all the calculations were done for the same total discharge energy and the efficiency of the radicals' production depends on E/N value only (Fig. 9). The major part of the discharge energy release happens during the high-current stage. E/N values in different regimes vary from 105 to 270 Td, which are close to the optimal conditions for molecules dissociation by electron impact in fuel-air mixtures [25]. However, it still can be observed that the H and O concentrations at low voltages, especially at 2000 V, are lower compared with the results at high voltage conditions, reflecting a small dissociation efficiency increase at higher E/N. As a result, the ignition efficiency by pulsed discharge is reduced at low pulse voltage. This comparison indicates that the enhancement in ignition kernel development by the vibrational excitation of $N_2(v = 1)$ through slow gas heating by VT relaxation is less efficient than the excitation of electronically excited species and the dissociation of H_2 and O_2 in producing radicals via kinetic enhancement pathways. The same results were obtained in previous works (see review [2]). It was shown that the relative efficiency of non-equilibrium dissociation and ionization of the gas compared to the efficiency of the heating of the mixture could be as high as 100. In paper [89], the optimal range of the E/N values for plasma enhanced ignition was indicated as $E/N \sim$ 200–300 Td, which is in a good agreement with the results of present work.

The corresponding thermal heating cases were compared with the plasma assisted ignition cases at different voltages. The electrode diameter and gap size of the cylindrical electrodes are 2.0 mm. It is assumed that the discharge energy deposited in the discharge channel is completely converted into gas heating without the radicals' formation. The results showed that the thermally-equilibrium ignition using the same amount of energy is impossible in all the range of parameters analyzed. This indicates the dominant roles of kinetics effects of plasma in ignition enhancement at initial temperatures close to the self-ignition threshold.

3.3. Effects of electrode geometry and heat loss on ignition

Besides the voltage effects, the electrode geometry also affects discharge properties and further ignition enhancement. In this section, the effects of electrode shape, electrode diameter, discharge gap size, and heat losses on the discharge development and ignition enhancement were studied.

3.3.1. Electrode shape

For the analysis of the electrodes' shape influence the plasma assisted ignition modeling was also conducted for parabolic and spherical shapes of electrodes. The minimum gap size remained at 2 mm. The length of parabolic or spherical parts of electrodes was

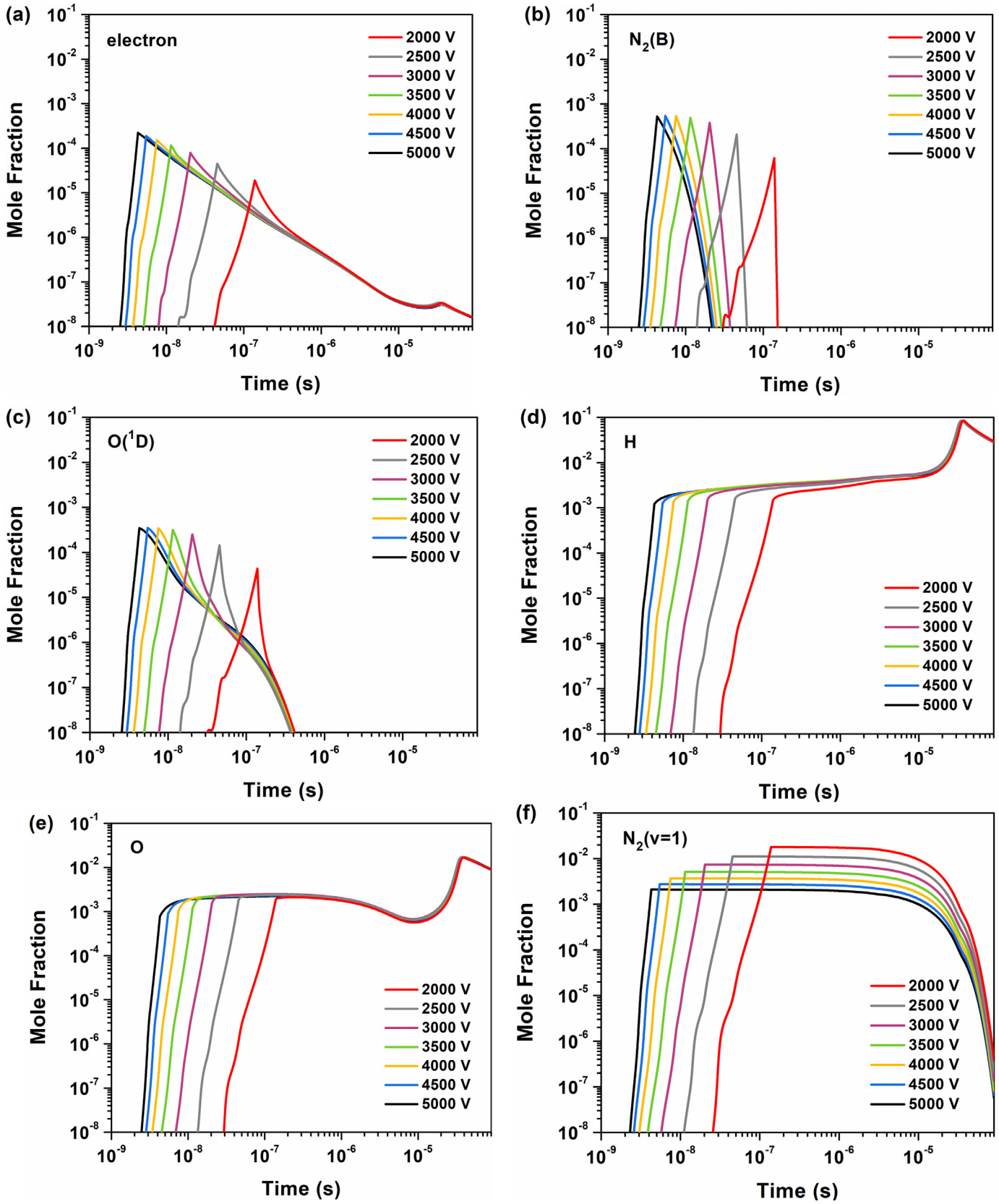

Fig. 9. Time evolutions of (a) electrons, electronically excited species (b) $N_2(B)$ and (c) $O(^1D)$, atoms (d) H and (e) O, as well as vibrationally excited species (f) $N_2(v = 1)$ with different pulse voltages at the location of ($R = 1$ mm, $Z = 5$ mm).

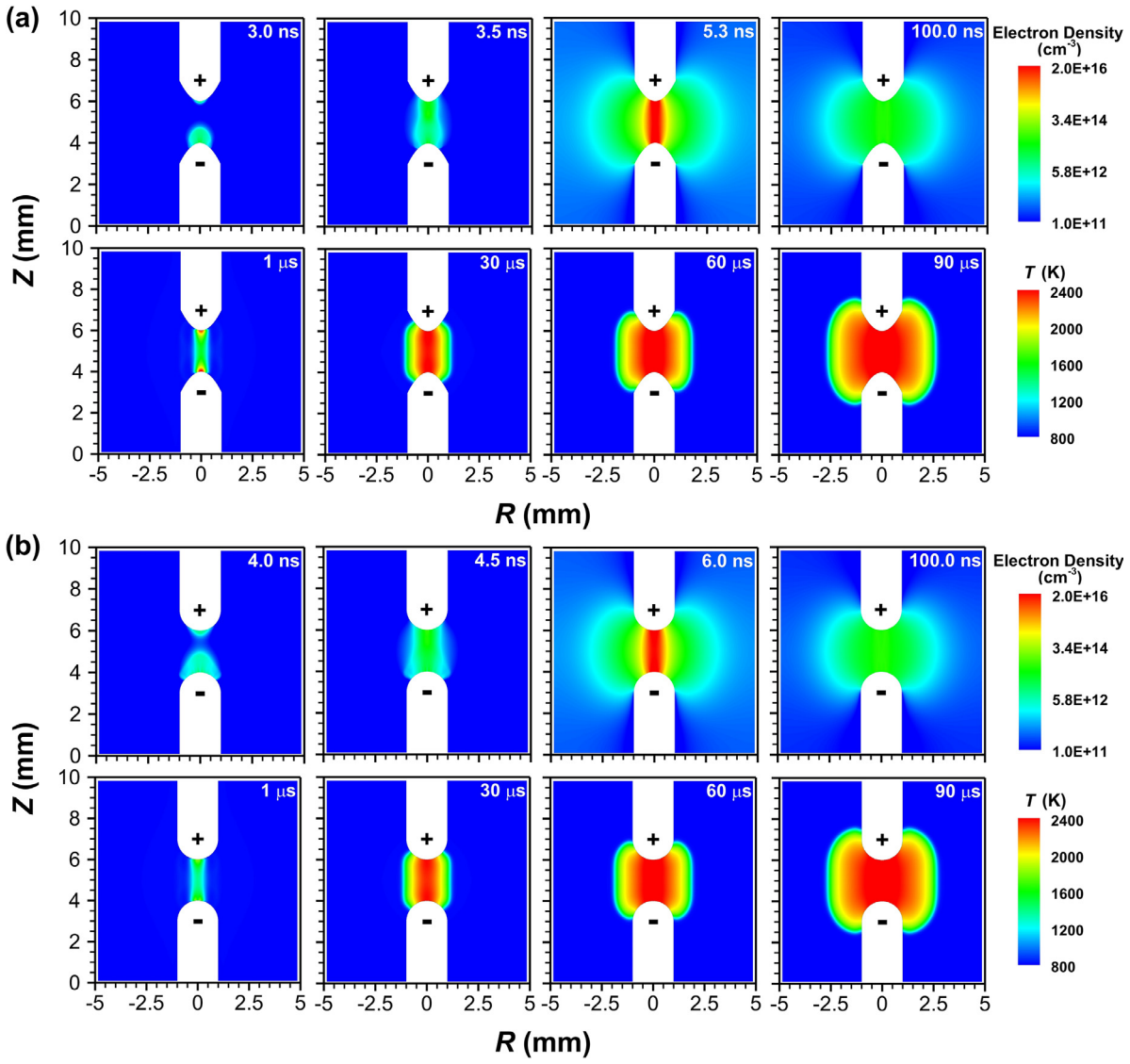

Fig. 10. Time evolutions of electron number density and gas temperature during plasma assisted H_2/air ignition with (a) parabolic and (b) spherical electrodes at $U = 5000$ V.

1 mm and the rest body of electrode remained cylindrical with a diameter of 2 mm, as shown in Fig. 10. The discharge voltage was kept at $U = 5000$ V with the rise time of 2 ns and the total deposited energy of 0.4 mJ.

Figures 10(a), (b) present the time evolution of electron number density and gas temperature during plasma assisted H_2/air ignition with parabolic and spherical electrodes. Compared with the flat head cylindrical electrodes, Fig. 10 shows that bridging the gap takes a longer time for the parabolic electrodes, followed by the spherical electrodes. The maximum E/N values after bridging the gap are similar for different electrode shapes due to the same discharge gap size. However, compared with the wide discharge channel and lower electron density produced between the cylindrical electrodes (Fig. 3(c)), a very narrow discharge channel with higher electron density is formed for the parabolic and spherical electrodes. The maximum electron density for the parabolic and spherical electrode discharge gaps is $n_e = 8.79\times10^{16}$ and 5.33×10^{16} cm^{-3} respectively due to higher specific energy deposited into plasma, compared with the $n_e = 1.73\times10^{16}$ cm^{-3} for cylindrical electrodes. Correspondingly, higher electron number density leads to faster production of excited species and radicals by electron impact during the discharge phase. From the temperature profiles (Fig. 10), it is observed that small ignition kernels are quickly formed at the tips of anode and cathode. Then, the ignition kernel propagates towards the unburned gas region from these hot spots.

Figure 11 shows the time evolutions of ignition kernel volume with different electrode shapes at $U = 5000$ V. The formation of initial flame kernel with parabolic and spherical electrodes is faster than in the case of cylindrical electrodes at $t < 30$ μs. This fast ignition occurs because of higher active species concentration and higher temperature in the narrow discharge channel near the axis of the discharge gap, as shown in Fig. 12. However, after the formation of initial ignition kernel at $t > 40$ μs (see Fig. 3(f)), the flame development in the case of cylindrical electrodes exceeds both cases of parabolic and spherical electrodes. These longer ignition delay time and faster flame development in the case of cylindrical electrodes are explained by smaller peak concentration of active species and smaller temperature increase, but much larger discharge volume (Fig. 12). This indicates that in addition to the electric field, a larger discharge volume with active species production is also critical to the ignition enhancement by plasma. It is interesting to note that when considering the heat loss from electrodes, the ignition kernel volume of parabolic electrodes is

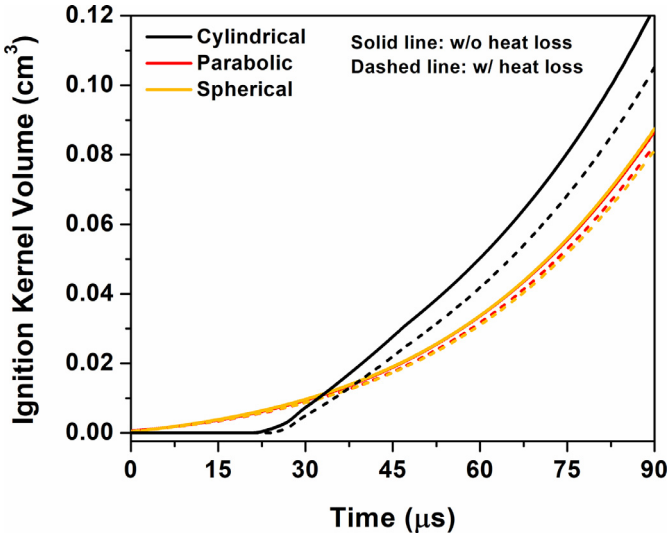

Fig. 11. Time evolutions of ignition kernel volume and total heat release with different electrode shapes at $U = 5000$ V.

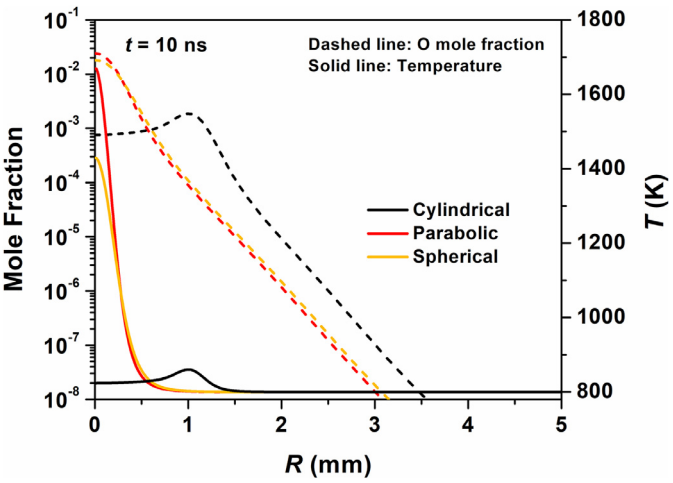

Fig. 12. Spatial distributions of atomic oxygen mole fraction and gas temperature at the center of electrode gap ($Z = 5$ mm) along R-axis for different electrode shapes at $t = 10$ ns after the discharge start.

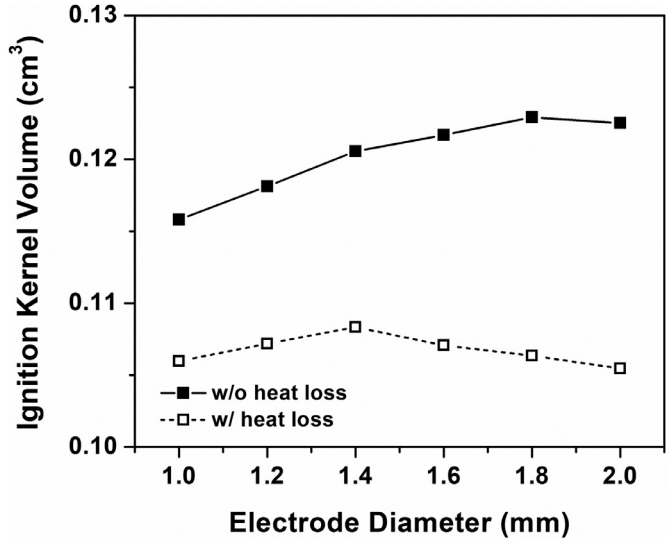

Fig. 14. Ignition kernel volume at $t = 90$ μs in plasma assisted H_2/air ignition with different electrode diameters at $U = 5000$ V.

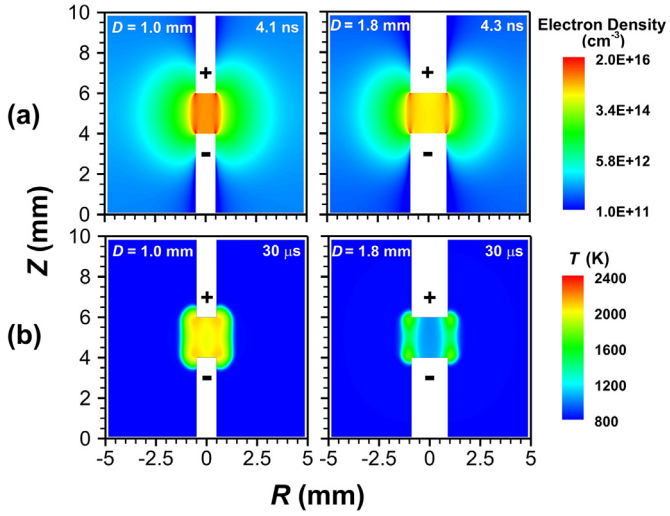

Fig. 15. (a) Electron number density at the end of discharge phase and (b) temperature profile at $t = 30$ μs for electrode diameter $D = 1.0$ and 1.8 mm.

bigger than that of spherical electrodes, while in the adiabatic case the ignition kernel is bigger for spherical electrodes. This is because a larger electrode surface area absorbs more heat from the flame kernel via convective heat transfer.

Heat loss on the electrodes leads to the quenching of ignition kernel. Compared to the adiabatic temperature profiles in Fig. 3(f) with the electrode diameter $D = 2.0$ mm, Fig. 13 shows the time evolution of gas temperature during plasma assisted H_2/air ignition taking into account the heat losses to electrode. It can be seen that the ignition kernel is quenched at the electrode surface and the development of ignition kernel is decelerated. The final ignition volume at $t = 90$ μs in Fig. 13 is by 14% smaller, demonstrating the effect of heat losses on the ignition development.

3.3.2. Electrode diameter

In this section, the effect of electrode diameter on ignition was studied. The modeling was performed using cylindrical electrodes

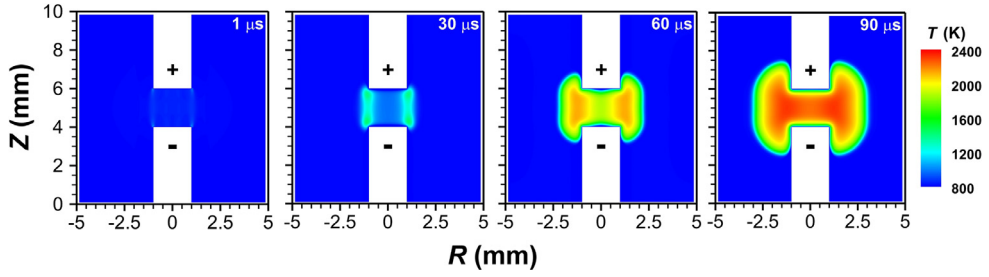

Fig. 13. Time evolution of gas temperature during plasma assisted H_2/air ignition with heat loss at $U = 5000$ V.

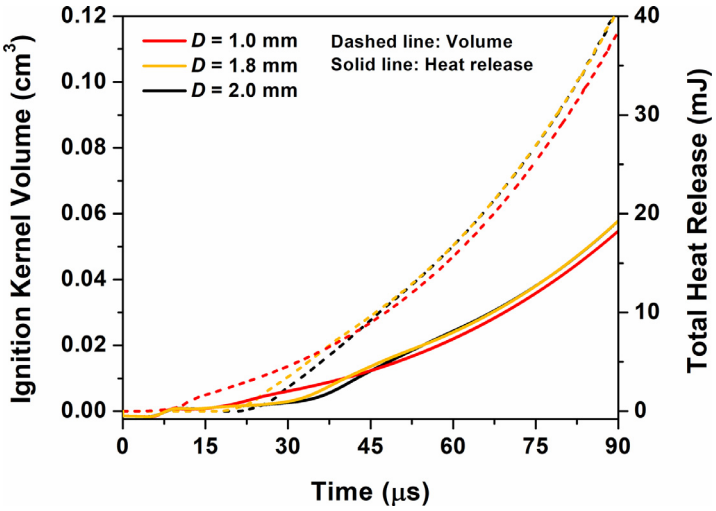

Fig. 16. Time evolutions of ignition kernel volume and total heat release with electrode diameter D = 1.0, 1.8 and 2.0 mm at U = 5000 V.

with the gap size of 2 mm. The electrode diameter was varied from 1.0 to 2.0 mm. The applied voltage was U = 5000 V and the same deposited energy of 0.4 mJ was applied for all conditions.

Figure 14 shows the ignition kernel volume at t = 90 μs for the different diameters of electrodes D. The calculations are conducted at the conditions with and without the heat loss to the electrodes. The results show that in the adiabatic case the maximum ignition kernel volume during 90 μs was reached with the electrodes' diameter D = 1.8 mm. Note that the heat loss to the electrodes reduces the optimum electrode diameter to D = 1.4 mm, indicating that the heat loss increases significantly with the electrode diameter and electrode surface area.

To illustrate the effects of electrode diameters on species production and temperature during the discharge and in ignition process, the analysis of plasma properties and active species production is conducted at the condition without heat loss. Fig. 15 shows the modeling results of electron number density at the end of the discharge phase and the temperature profile at t = 30 μs for the electrode diameter of D = 1.0 and 1.8 mm, respectively. The electron density is higher in the case D = 1.0 mm (Fig. 15(a)) due to smaller diameter of the plasma channel and higher value of the specific energy deposited (compare also with the results at D = 2.0 mm shown in Fig. 3(c)). Therefore, the initial ignition kernel is formed in the discharge gap faster when the electrode diameter is smaller, as shown in Fig. 15(b).

Figure 16 shows the time evolution of ignition kernel volume and total heat release for different electrode diameters of D = 1.0, 1.8, and 2.0 mm. The results show that the growth of initial kernel volume (t < 30 μs) is faster for the electrode diameter of 1.0 mm. However, the ignition kernel volume for D = 1.8 mm becomes the largest after t = 45 μs. For the electrode diameter of 2.0 mm, the ignition kernel volume and heat release at t = 45 μs exceed the results at D = 1.0 mm, but still remain lower than those that for D = 1.8 mm. Even though a larger discharge volume is generated in the case of D = 2.0 mm, the lower active species concentrations and smaller temperature increase produced by discharge decelerate the ignition development. Fig. 17 shows the spatial distributions of atomic oxygen and temperature at the center of electrode gap (Z = 5 mm) with different electrode diameters at t = 10 ns after the discharge start. Higher concentration of active species is generated for D = 1.8 mm and leads to the maximum ignition enhancement with the same discharge energy. The discussion above indicates that an optimum electrode diameter exists at which the maximum ignition enhancement could be achieved.

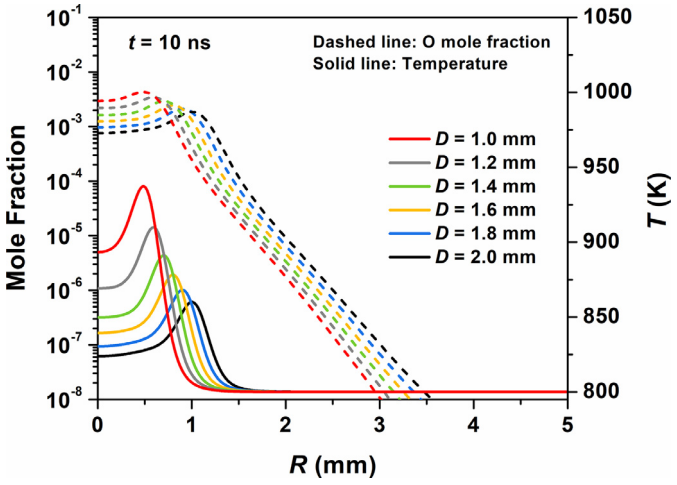

Fig. 17. Spatial distribution of atomic oxygen and gas temperature at the center of electrode gap (Z = 5 mm) along R-axis for different electrode diameters at t = 10 ns after the discharge start.

3.3.3. Electrode gap size

In this section, the plasma assisted H_2/air ignition with different electrode gap sizes L was studied. The electrode shape was cylindrical with the diameter of D = 2 mm. The gap size was varied from 0.6 to 2.0 mm. The applied voltage was U = 2000 V to avoid very high E/N in a small gap. The deposited energy was 0.4 mJ for all calculations.

Fig. 18 shows the ignition kernel volume at t = 90 μs for different electrode gap sizes. The results show that the ignition kernel volume increases with the gap size decrease, and reaches its maximum at L = 0.8 mm without heat loss. Further decrease of the gap size decreases the ignition kernel volume. With heat loss, the optimum electrode gap size becomes L = 1.0 mm. Thus, the heat loss limits the ignition kernel development at small gap size.

Figure 19 presents the 2D modeling results of atomic oxygen mole fraction at the end of the discharge phase and gas temperature distribution at t = 30 μs for gap size of 0.6, 0.8 and 2 mm, respectively, for a zero heat loss case. The results show that the ignition kernel was developed quickly for gap size of 0.6 and 0.8 mm.

The ignition development is affected by both the discharge volume and species concentrations produced in plasma. The decrease of electrode gap size results in more discharge energy deposited

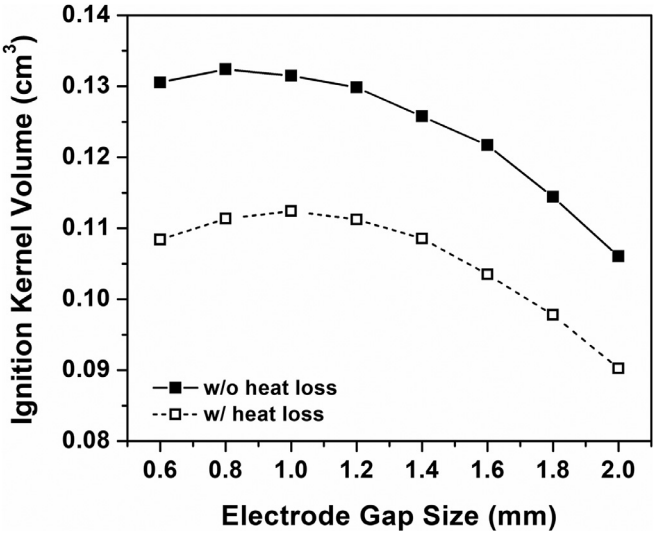

Fig. 18. Ignition kernel volume at $t = 90$ μs in the plasma assisted H_2/air ignition with different electrode gap sizes at $U = 2000$ V.

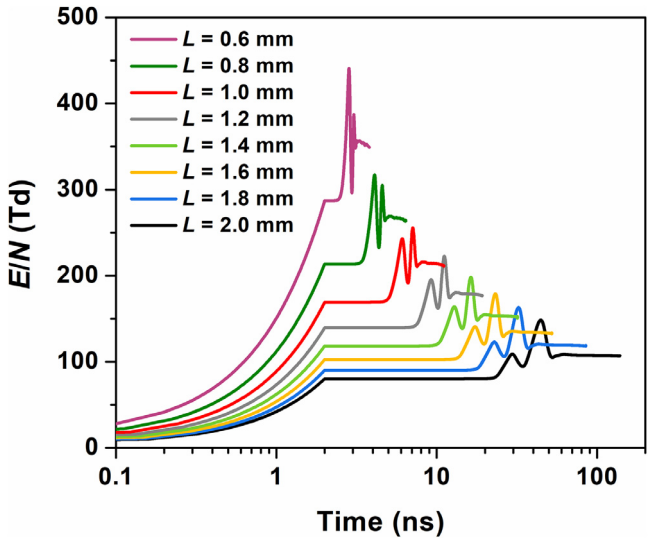

Fig. 20. Time evolutions of E/N at the location of ($R = 1$ mm, $Z = 5$ mm) at $U = 2000$ V.

into a smaller volume and an increase of active species concentrations in the gap. In addition, the change of electrode gap size also affects the E/N values and species production in the discharge. Figure 20 shows that the time evolutions of E/N at the coordinates of ($R = 1$ mm, $Z = 5$ mm). The E/N increase further promotes the production of electronically excited species and radicals which are more efficient in ignition enhancement than vibrationally and rotationally excited species produced at low E/N conditions. For the active species production in plasma, Fig. 21 shows atomic oxygen mole fraction and temperature along R-axis at the center of electrode gap ($Z = 5$ mm) with different electrode gap sizes at $t = 150$ ns after discharge start for all conditions. The atomic oxygen mole fraction near the electrode edges for a gap size of 0.8 mm is about 5.7 times higher compared with the 2 mm gap. When the gap size drops below 0.8 mm, the decrease of discharge volume turns to be the dominant factor and decreases the efficiency of ignition.

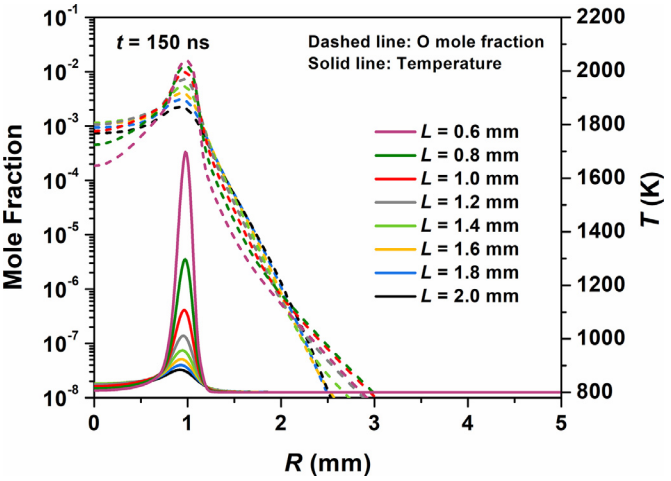

Fig. 21. Spatial distribution of atomic oxygen mole fraction and temperature at the center of the discharge gap ($Z = 5$ mm) along R-axis for different electrode gap sizes at $t = 150$ ns after the discharge start.

4. Conclusion

This work investigated the effects of non-equilibrium excitation and electrode geometries on H_2/air ignition in a nanosec-

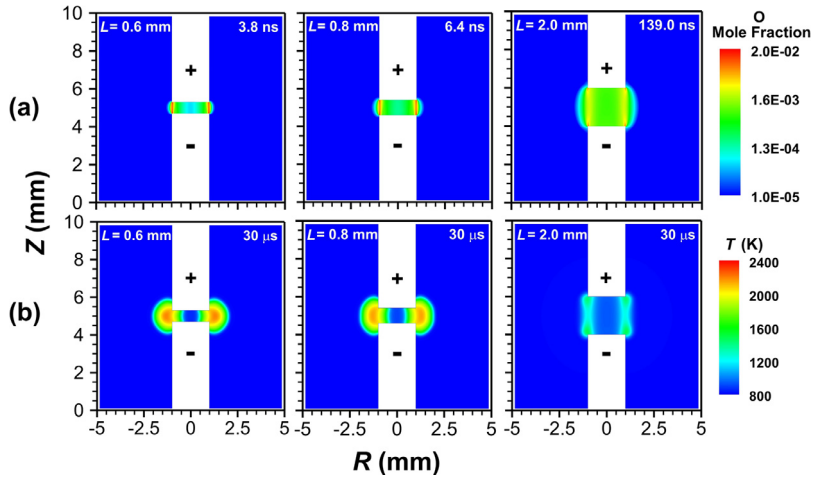

Fig. 19. (a) Atomic oxygen mole fraction at the end of discharge phase, and (b) temperature profile at $t = 30$ μs for inter-electrode gap size $L = 0.6$, 0.8 and 2.0 mm.

ond plasma discharge by two-dimensional simulation. By integrating the BOLSIG+ electron kinetics solver, 2D PASSKEy plasma solver and the unsteady, compressible and multi-component reactive flow solver ASURF+, a new multi-scale adaptive reduced chemistry solver for plasma assisted combustion (MARCS-PAC) was developed.

The effects of non-equilibrium plasma excitation, discharge gap geometry and heat loss on the ignition kernel development were studied using this model with detailed combustion chemistry and transport. The results show that the production of electronically excited species (N_2(A), N_2(B), N_2(a′), N_2(C), and O(^{1}D)) and ground-state atoms H and O at high reduced electric field significantly promote the ignition kernel development. Vibrational excitation is less efficient than the electronical excitation and dissociation. Fast gas heating mechanism plays a major role in temperature increase during nanosecond discharge phase and early afterglow.

The non-uniform distributions of plasma properties and active species, such as *E*/*N* and temperature, as well as electrons, excited species and radicals are demonstrated by the 2D simulations. The localized discharges initiated near the sharp edges of electrodes generate 'hot spots' with high concentration of active species, higher temperature and promote the ignition kernel development.

It was shown that the plasma-assisted ignition is significantly affected by the electrode geometry including electrode shape, diameter and gap size because of the redistribution of the electric field and the plasma density. A larger discharge volume and further ignition kernel volume are formed with the cylindrical electrodes compared with the parabolic and spherical head tops, indicating that a larger discharge volume with active species production is also critical to the ignition enhancement in addition to the electric field. It was shown that the optimal discharge gap geometry allows reaching the maximum ignition enhancement with the same discharge energy.

Finally, it was shown that the heat loss through electrodes significantly slows down the ignition kernel development. The ignition kernel volume is significantly reduced at a larger electrode surface area, electrode diameter and smaller electrode gap size. This conclusion modifies the optimal electrodes' geometry for the efficient ignition enhancement, and increases the non-monotonic dependence of ignition dynamics on the discharge gap geometry, high-voltage pulse amplitude and duration.

Declaration of Competing Interest

The authors declare that they have no known competing financial interests or personal relationships that could have appeared to influence the work reported in this paper.

Acknowledgments

This work was partly supported by the grants of DOE Plasma Science Center (DE-SC0020233) and National Science Foundation (CBET-1903362 and NSF-EFRI CBET-2029425). The authors would like to thank the great help of the young research group at Atelier des Plasmas in implementing the PASSKEy solver. The simulations presented in this article were performed on computational resources supported by the Princeton Institute for Computational Science and Engineering (PICSciE) and the Office of Information Technology's High Performance Computing Center and Visualization Laboratory at Princeton University.

Supplementary materials

Supplementary material associated with this article can be found, in the online version, at doi:10.1016/j.combustflame.2022.112046.

References

[1] A. Starikovskiy, J. Leon Shohet, High E/N Discharges: Applications. Encyclopedia of Plasma Technology, CRC Press, 2016.
[2] A. Starikovskiy, N. Aleksandrov, Plasma-assisted ignition and combustion, Prog. Energy Combust. Sci. 39 (2013) 61–110.
[3] Y. Ju, W. Sun, Plasma assisted combustion: dynamics and chemistry, Prog. Energy Combust. Sci. 48 (2015) 21–83.
[4] A. Starikovskiy, N. Aleksandrov, A. Rakitin, Plasma-assisted ignition and deflagration-to-detonation transition, Phil. Trans. R. Soc. A 370 (2012) 740–773.
[5] J.K. Lefkowitz, P. Guo, T. Ombrello, S.H. Won, C.A. Stevens, J.L. Hoke, F. Schauer, Y. Ju, Schlieren imaging and pulsed detonation engine testing of ignition by a nanosecond repetitively pulsed discharge, Combust. Flame 162 (2015) 2496–2507.
[6] I. Dunn, K.A. Ahmed, R.J. Leiweke, T. Ombrello, Optimization of flame kernel ignition and evolution induced by modulated nanosecond-pulsed high-frequency discharge, Proc. Combust. Inst. 38 (2021) 6541–6550.
[7] H. Zhao, N. Zhao, T. Zhang, S. Wu, G. Ma, C. Yan, Y. Ju, Studies of multi-channel spark ignition of lean n-pentane/air mixtures in a spherical chamber, Combust. Flame 212 (2020) 337–344.
[8] J. Choe, W. Sun, T. Ombrello, C. Carter, Plasma assisted ammonia combustion: simultaneous NOx reduction and flame enhancement, Combust. Flame 228 (2021) 430–432.
[9] G. Vignat, N. Minesi, P.R. Soundararajan, D. Durox, A. Renaud, V. Blanchard, C.O. Laux, S. Candel, Improvement of lean blow out performance of spray and premixed swirled flames using nanosecond repetitively pulsed discharges, Proc. Combust. Inst. 38 (2021) 6559–6566.
[10] A. Starikovskiy, N. Anikin, I. Kosarev, E. Mintoussov, M. Nudnova, A. Rakitin, D. Roupassov, S. Starikovskaia, V. Zhukov, Nanosecond-pulsed discharges for plasma-assisted combustion and aerodynamics, J. Propuls. Power 24 (2008) 1182–1197.
[11] A. Nikipelov, I. Popov, G. Correale, A. Rakitin, A. Starikovskiy, Ultra–lean and ultra–rich flames stabilization by high–voltage nanosecond pulsed discharge, Proceedings of the 48th AIAA Aerospace Sciences Meeting, Jan, Orlando, Florida (2010) Paper AIAA-2010-1341.
[12] J. Sun, Y. Tang, S. Li, Plasma-assisted stabilization of premixed swirl flames by gliding arc discharges, Proc. Combust. Inst. 38 (2021) 6733–6741.
[13] H. Zhong, X. Mao, A.C. Rousso, C.L. Patrick, C. Yan, W. Xu, Q. Chen, G. Wysocki, Y. Ju, Kinetic study of plasma-assisted n-dodecane/O_2/N_2 pyrolysis and oxidation in a nanosecond-pulsed discharge, Proc. Combust. Inst. 38 (2021) 6521–6531.
[14] A.C. Rousso, B.M. Goldberg, T.Y. Chen, S. Wu, A. Dogariu, R.B. Miles, E. Kolemen, Y. Ju, Time and space resolved diagnostics for plasma thermal-chemical instability of fuel oxidation in nanosecond plasma discharges, Plasma Sources Sci. Technol. 29 (2020) 105012.
[15] R. Zhang, H. Liao, J. Yang, B. Yang, Exploring chemical kinetics of plasma assisted oxidation of dimethyl ether (DME), Combust. Flame 225 (2021) 388–394.
[16] N.B. Anikin, S.M. Starikovskaia, A.Y. Starikovskiy, Oxidation of saturated hydrocarbons under the effect of nanosecond pulsed space discharge, J. Phys. D Appl. Phys. 39 (2006) 3244–3252.
[17] S.M. Starikovskaia, A.Y. Starikovskiy, D.V. Zatsepin, Hydrogen oxidation in stoichiometric hydrogen-air mixtures in the fast ionization wave, Combust. Theory Model. 5 (2001) 97–129.
[18] N.B. Anikin, S.M. Starikovskaia, A.Y. Starikovskiy, Study of the oxidation of alkanes in their mixtures with oxygen and air under the action of a pulsed volume nanosecond discharge, Plasma Phys. Rep. 30 (2004) 1028–1042.
[19] X. Mao, Q. Chen, C. Guo, Methane pyrolysis with N_2/Ar/He diluents in a repetitively-pulsed nanosecond discharge: kinetics development for plasma assisted combustion and fuel reforming, Energy Convers. Manag. 200 (2019) 112018.
[20] T.Y. Chen, T.S. Taneja, A.C. Rousso, S. Yang, E. Kolemen, Y. Ju, Time-resolved *in situ* measurements and predictions of plasma-assisted methane reforming in a nanosecond-pulsed discharge, Proc. Combust. Inst. 38 (2021) 6533–6540.
[21] J. Sun, Q. Chen, Y. Guo, Z. Zhou, Y. Song, Quantitative behavior of vibrational excitation in AC plasma assisted dry reforming of methane, J. Energy Chem. 46 (2020) 133–143.
[22] A.A. Nikipelov, A.E. Rakitin, I.B. Popov, G. Correale, A.Y. Starikovskiy, Compact and power–intensive catalyst–free partial oxidation reformer of liquid fuels to syngas, Proceedings of the 49th AIAA Aerospace Sciences Meeting, Jan, Orlando, Florida (2011) Paper AIAA-2011-1332.
[23] Y. Ju, J.K. Lefkowitz, C.B. Reuter, S.H. Won, X. Yang, S. Yang, W. Sun, Z. Jiang, Q. Chen, Plasma assisted low temperature combustion, Plasma Chem. Plasma Process 36 (2016) 85–105.
[24] S. Pancheshnyi, A. Nikipelov, E. Anokhin, A. Starikovskiy, SI engine with repetitive ns spark plug, Proceedings of the 52nd Aerospace Sciences Meeting AIAA (2014) Paper 2014-1182.
[25] A.Y. Starikovskiy, Plasma supported combustion, Proc. Combust. Inst. 30 (2005) 2405–2417.

[26] S.M. Starikovskaia, Plasma-assisted ignition and combustion: nanosecond discharges and development of kinetic mechanisms, J. Phys. D Appl. Phys. 47 (2014) 353001 34.
[27] X. Mao, Q. Chen, A.C. Rousso, T.Y. Chen, Y. Ju, Effects of controlled non-equilibrium excitation on H_2/O_2/He ignition using a hybrid repetitive nanosecond and DC discharge, Combust. Flame 206 (2019) 522–535.
[28] X. Mao, A. Rousso, Q. Chen, Y. Ju, Numerical modeling of ignition enhancement of CH_4/O_2/He mixtures using a hybrid repetitive nanosecond and DC discharge, Proc. Combust. Inst. 37 (2019) 5545–5552.
[29] J.K. Lefkowitz, P. Guo, A. Rousso, Y. Ju, Species and temperature measurements of methane oxidation in a nanosecond repetitively pulsed discharge, Phil. Trans. R. Soc. A 373 (2015) 20140333.
[30] Y. Wang, P. Guo, H. Chen, Z. Chen, Numerical modeling of ignition enhancement using repetitive nanosecond discharge in a hydrogen/air mixture I: calculations assuming homogeneous ignition, J. Phys. D Appl. Phys. 54 (2021) 065501 (12pp).
[31] H. Zhong, M.N. Shneider, X. Mao, Y. Ju, Dynamics and chemical mode analysis of plasma thermal-chemical instability, Plasma Sources Sci. Technol. 30 (2021) 035002 16pp.
[32] H. Zhong, M.N. Shneider, M.S. Mokrov, Y. Ju, Thermal-chemical instability of weakly ionized plasma in a reactive flow, J. Phys. D Appl. Phys. 52 (2019) 484001 9pp.
[33] S. Yang, S. Nagaraja, W. Sun, V. Yang, Multiscale modeling and general theory of non-equilibrium plasma-assisted ignition and combustion, J. Phys. D Appl. Phys. 50 (2017) 433001 18pp.
[34] S. Nagaraja, V. Yang, Z. Yin, I. Adamovich, Ignition of hydrogen–air mixtures using pulsed nanosecond dielectric barrier plasma discharges in plane-to-plane geometry, Combust. Flame 161 (2014) 1026–1037.
[35] R. Mahamud, A.A. Tropina, M.N. Shneider, R.B. Miles, Dual-pulse laser ignition model, Phys. Fluids. 30 (2018) 10610.
[36] S. Kobayashi, Z. Bonaventura, F. Tholin, N.A. Popov, A. Bourdon, Study of nanosecond discharges in H_2–air mixtures at atmospheric pressure for plasma assisted combustion applications, Plasma Sources Sci. Technol. 26 (2017) 075004.
[37] F. Tholin, D. Lacoste, A. Bourdon, Influence of fast-heating processes and O atom production by a nanosecond spark discharge on the ignition of a lean H_2–air premixed flame, Combust. Flame 161 (2014) 1235–1246.
[38] A. Sharma, V. Subramaniam, E. Solmaz, L.L. Raja, Fully coupled modeling of nanosecond pulsed plasma assisted combustion ignition, J. Phys. D Appl. Phys. 52 (2019) 095204.
[39] N.B. Anikin, E.I. Mintoussov, S.V. Pancheshnyi, D.V. Roupassov, V.E. Sych, A.Y. Starikovskiy, Nonequilibrium plasmas and its applications for combustion and hypersonic flow control, Proceeding of the 41st AIAA Aerospace Sciences Meeting and Exhibit, 2003 Paper AIAA 2003-1053.
[40] Y. Bechane, B. Fiorina, Numerical investigations of turbulent premixed flame ignition by a series of nanosecond repetitively pulsed discharges, Proc. Combust. Inst. 38 (2021) 6575–6582.
[41] M. Castela, B. Fiorina, A. Coussement, O. Gicquel, N. Darabiha, C.O. Laux, Modelling the impact of non-equilibrium discharges on reactive mixtures for simulations of plasma-assisted ignition in turbulent flows, Combust. Flame 166 (2016) 133–147.
[42] M. Castela, S. Stepanyan, B. Fiorina, A. Coussement, O. Gicquel, N. Darabiha, C.O. Laux, A 3-D DNS and experimental study of the effect of the recirculating flow pattern inside a reactive kernel produced by nanosecond plasma discharges in a methane-air mixture, Proc. Combust. Inst. 36 (2017) 4095–4103.
[43] A. Lo, F. Frat, E. Domingues, A. Lacour, B. Lecordier, P. Vervisch, A. Cessou, Nanosecond pulsed discharge in a propane–air mixture: ignition and energy deposition, Proc. Combust. Inst. 36 (2017) 4087–4094.
[44] S.V. Pancheshnyi, D.A. Lacoste, A. Bourdon, C.O. Laux, Ignition of propane–air mixtures by a repetitively pulsed nanosecond discharge, IEEE Trans. Plasma Sci. 34 (2006) 2478–2487.
[45] J.K. Lefkowitz, T. Ombrello, An exploration of inter-pulse coupling in nanosecond pulsed high frequency discharge ignition, Combust. Flame 180 (2017) 136–147.
[46] J.K. Lefkowitz, T. Ombrello, Reduction of flame development time in nanosecond pulsed high frequency discharge ignition of flowing mixtures, Combust. Flame 193 (2018) 471–480.
[47] Y. Zhu, X. Chen, Y. Wu, S. Starikovskaia. PASSKEy code [software]. Available from http://www.plasma-tech.net/parser/passkey/(Science and Technology of Plasma Dynamics Laboratory, Xi'an, China and Laboratoire de Physique des Plasmas, Paris, France, 2021).
[48] X. Chen, Y. Zhu, Y. Wu, Modeling of streamer-to-spark transitions in the first pulse and the post discharge stage, Plasma Sources Sci. Technol. 29 (2020) 095006 17pp.
[49] Y. Zhu, S. Shcherbanev, B. Baron, S. Starikovskaia, Nanosecond surface dielectric barrier discharge in atmospheric pressure air: I. Measurements and 2D modeling of morphology, propagation and hydrodynamic perturbations, Plasma Sources Sci. Technol. 26 (2017) 125004.
[50] X. Chen, Y. Zhu, Y. Wu, J. Hao, X. Ma, P. Lu, Modeling of fast ionization waves in pure nitrogen at moderate pressure, Plasma Sources Sci. Technol. 30 (2021) 065002.
[51] X. Chen, Y. Zhu, Y. Wu, J. Hao, X. Ma, P. Lu, Numerical investigations of nanosecond surface streamers at elevated pressure, Plasma Sources Sci. Technol. 30 (2021) 075008.
[52] Y. Zhu, X. Chen, Y. Wu, J. Hao, X. Ma, P. Lu, P. Tardiveau, Simulation of the ionization wave discharges: a direct comparison between the fluid model and E–FISH measurements, Plasma Sources Sci. Technol. 30 (2021) 075025.
[53] Z. Chen, Studies on the Initiation, Propagation, and Extinction of Premixed Flames, The Department of Mechanical and Aerospace Engineering, Princeton University, Princeton, NJ, 2009.
[54] Z. Chen, M.P. Burke, Y. Ju, Effects of Lewis number and ignition energy on the determination of laminar flame speed using propagating spherical flames, Proc. Combust. Inst. 32 (2009) 1253–1260.
[55] W. Sun, Developments of Efficient Numerical Methods for Combustion Modeling with Detailed Chemical Kinetics, The Department of Mechanical and Aerospace Engineering, Princeton University, Princeton, NJ, 2020.
[56] T. Zhang, W. Sun, L. Wang, Y. Ju, Effects of low-temperature chemistry and turbulent transport on knocking formation for stratified dimethyl ether/air mixtures, Combust. Flame 200 (2019) 342–353.
[57] A. Bourdon, V.P. Pasko, N.Y. Liu, S. Célestin, P. Ségur, E. Marode, Efficient models for photoionization produced by non-thermal gas discharges in air based on radiative transfer and the Helmholtz equations, Plasma Sources Sci. Technol. 16 (2007) 656–678.
[58] A. Luque, U. Ebert, C. Montijn, W. Hundsdorfer, Photoionization in negative streamers: fast computations and two propagation modes, Appl. Phys. Lett. 90 (2007) 081501.
[59] A. Flitti, S. Pancheshnyi, Gas Heating in Fast Pulsed Discharges in N_2–O_2 Mixtures, Eur. Phys J. Appl. Phys. 45 (2009) 21001.
[60] G.J.M. Hagelaar, L.C. Pitchford, Solving the Boltzmann equation to obtain electron transport coefficients and rate coefficients for fluid models, Plasma Sources Sci. Technol. 14 (2005) 722–733.
[61] S. Pancheshnyi, S. Biagi, M.C. Bordage, G.J.M. Hagelaar, W.L. Morgan, A.V. Phelps, L.C. Pitchford, The lxcat project: electron scattering cross sections and swarm parameters for low temperature plasma modeling, Chem. Phys. 398 (2012) 148–153.
[62] M. Černák, T. Hoder, Z. Bonaventura, Streamer breakdown: cathode spot formation, Trichel pulses and cathode-sheath instabilities, Plasma Sources Sci. Technol. 29 (2020) 013001.
[63] R.J. Kee, J.F. Grcar, M.D. Smooke, J.A. Miller, PREMIX: a FORTRAN program for modeling steady laminar one-dimensional premixed flames, Report No. SAND-85-8240, Sandia National Laboratories, Livermore, CA, USA, 1985.
[64] P. Sonneveld, CGS, a fast lanczos-type solver for nonsymmetric linear systems, SIAM J. Sci. Stat. Comput. 10 (1989) 36–52.
[65] O. Schenk, K. Gärtner, Solving unsymmetric sparse systems of linear equations with PARDISO, Future Gener. Comput. Syst. 20 (2004) 475–487.
[66] P.L.G. Ventzek, T.J. Sommerer, R.J. Hoekstra, M.J. Kushner, Two-dimensional hybrid model of inductively coupled plasma sources for etching, Appl. Phys. Lett. 63 (1993) 605–607.
[67] A. Villa, L. Barbieri, M. Gondola, R. Malgesini, An asymptotic preserving scheme for the streamer simulation, J. Comput. Phys. 242 (2013) 86–102.
[68] J.G. Li, Upstream nonoscillatory advection schemes, Mon. Weather Rev. 136 (2008) 4709–4729.
[69] J.G. Verwer, B.P. Sommeijer, W. Hundsdorfer, RKC time-stepping for advection–diffusion–reaction problems, J. Comput. Phys. 201 (2004) 61–79.
[70] R.J. Kee, F.M. Rupley, J.A. Miller, Chemkin-II: a fortran chemical kinetics package for the analysis of gas-phase chemical kinetics, Report No. SAND-89-8009, Sandia National Laboratories, Livermore, CA, USA, 1989.
[71] E.F. Toro, Riemann Solvers and Numerical Methods For Fluid Dynamics: A Practical Introduction, Springer-Verlag, Berlin Heidelberg, 1999.
[72] G.S. Jiang, C.W. Shu, Efficient implementation of weighted ENO schemes, J. Comput. Phys. 126 (1996) 202–228.
[73] C.W. Shu, High Order ENO and WENO Schemes for Computational Fluid, High-order Methods For Computational Physics, Springer, Berlin, Heidelberg, 1999.
[74] W. Sun, Y. Ju, A multi-timescale and correlated dynamic adaptive chemistry and transport (CO-DACT) method for computationally efficient modeling of jet fuel combustion with detailed chemistry and transport, Combust. Flame 184 (2017) 297–311.
[75] X. Gou, W. Sun, Z. Chen, Y. Ju, A dynamic multi-timescale method for combustion modeling with detailed and reduced chemical kinetic mechanisms, Combust. Flame 157 (2010) 1111–1121.
[76] Phelps database, www.lxcat.net, retrieved on July 1, 2020.
[77] Biagi database, www.lxcat.net, retrieved on July 1, 2020.
[78] IST-Lisbon database, www.lxcat.net, retrieved on July 1, 2020.
[79] X. Yang, X. Shen, J. Santner, H. Zhao, Y. Ju, Princeton HP-Mech. http://engine.princeton.edu/mechanism/HP-Mech.html, 2017.
[80] H. Zhao, L. Wu, C. Patrick, Z. Zhang, Y. Rezgui, X. Yang, G. Wysocki, Y. Ju, Studies of low temperature oxidation of n-pentane with nitric oxide addition in a jet stirred reactor, Combust. Flame 197 (2018) 78–87.
[81] P. Gokulakrishnan, C.C. Fuller, M.S. Klassen, Experimental and modeling study of C1–C3 hydrocarbon ignition in the presence of nitric oxide, J. Eng. Gas Turbines Power 140 (2018) 041509.
[82] H. Zhao, X. Yang, Y. Ju, Kinetic studies of ozone assisted low temperature oxidation of dimethyl ether in a flow reactor using molecular-beam mass spectrometry, Combust. Flame 173 (2016) 187–194.
[83] S. Pancheshnyi, Role of electronegative gas admixtures in streamer start, propagation and branching phenomena, Plasma Sources Sci. Technol. 14 (2005) 645–653.
[84] F. Tholin, A. Bourdon, Simulation of the hydrodynamic expansion following a nanosecond pulsed spark discharge in air at atmospheric pressure, J. Phys. D Appl. Phys. 46 (2013) 365205 18pp.

[85] N.A. Popov, Investigation of the mechanism for rapid heating of nitrogen and air in gas discharges, Plasma Phys. Rep. 27 (2001) 886–896.
[86] N.A. Popov, Fast gas heating in a nitrogen-oxygen discharge plasma: I. Kinetic mechanism, J. Phys. D Appl. Phys. 44 (2011) 285201.
[87] M.M. Nudnova, S.V. Kindysheva, N.L. Aleksandrov, A.Y. Starikovskiy, Fast gas heating in N_2/O_2 mixtures under nanosecond surface dielectric barrier discharge: the effects of gas pressure and composition, Phil. Trans. R. Soc. A 373 (2015) 20140330.
[88] N.L. Aleksandrov, S.V. Kindysheva, M.M. Nudnova, A.Y. Starikovskiy, Mechanism of ultra-fast heating in a nonequilibrium weakly-ionized air discharge plasma in high electric fields, J. Phys. D Appl. Phys. 43 (2010) 255201.
[89] N.L. Aleksandrov, N.B. Anikin, E.M. Bazelyan, D.V. Zatsepin, S.M. Starikovskaia, A.Y. Starikovskiy, Chemical reactions and ignition initiation in hydrocarbon-air mixtures by high-voltage nanosecond gas discharge, Proceedings of the 32nd AIAA Plasmadynamics and Lasers Conference, Anaheim, CA (2001) 2001-2949.